The South Tibet Detachment shear zone in the Dinggye area. Time constraints on extrusion models of the Himalayas.

P.H. Leloup (1); G. Mahéo (1); N. Arnaud (2); E. Kali (3); E. Boutonnet (1); Dunyi Liu (4); Liu Xiaohan (5); Li Haibing (4).

(1) CNRS UMR 5570 Université Lyon1 - ENS Lyon, Villeurbanne, France.

(2) Géosciences Montpellier, Université de Montpellier2, Montpellier France.

(3) Institut de Physique du Globe de Strasbourg (CNRS, UdS/EOST), UMR 7516, Strasbourg, France.

(4) Laboratory of Continental Dynamics, Institute of Geology, CAGS, Beijing, China

(5) Institute of Tibetan Plateau Research, Chinese Academy of Sciences, Beijing, China

Abstract

We investigate the timing of end of motion along the South Tibet detachment system (STDS), a major normal fault system that runs parallel to the Himalayan range for more than 1500km. Near Dinggye (~ 28°10'N, 87°40'E), the STD dips ~10±5° to the North and separates Paleozoic Tethyan series from Upper Himalayan Crystalline Series (UHCS). Immediately below the STD, the UHCS is highly deformed in the STD shear zone, lineations trend NNE and the shear senses are top to the NE. In micaschist, P-T path constrained by pseudosection and garnet chemistry, shows successive metamorphic conditions of ~0.6 GPa and ~550°C and 0.5 GPa and 625°C. U/Pb dating of Monazite and zircons in deformed and undeformed leucogranites suggest that ductile deformation lasted until at least ~16 Ma but ended prior to ~15Ma in the STD shear zone ~100 meters below the detachment. Ar/Ar micas ages in the footwall span between ~14.6 and 13.6 Ma, indicating rapid cooling down to ~320°C, and suggesting persistence of normal faulting, at that time. The STDS is cut and offset by the N-S trending Dinggye active normal fault which initiated prior to 11Ma thus providing a minimum bound for the end of STDS motion. These data are interpreted as reflecting 0.3 GPa (11km) to 0.6 GPa (22km) of exhumation along the STDS starting prior to ~16 Ma, ending between 13.6 and 11 Ma. The 1000 km long stretch of the STDS east of the Gurla Mandata probably stopped almost synchronously between 13 and 11 Ma ago, coevally with a sudden switch from NNE-SSW to E-W extension at the top of the accretionary prism, with jump of the major thrust from the lower Main Central Thrust (MCTl) to the Main the Boundary Thrust (MBT), and with change in India and Asia convergence direction. This synchronism is probably better explain in the frame of a thrust wedge or thrust system model than a lower channel flow model. West of the Gurla Mandata the STDS appears to stop 5 to 3 Ma earlier, possibly related to local interactions with the Karakorum fault in a way that needs to be understand.

1 Introduction

Since its discovery the South Tibet detachment system (STDS) has drove the attention of many scientists as this major structure that parallel for more than

1500 km the Himalayan range, which is the archetype of a compressive thrust belt, shows normal faulting in a direction almost parallel to the direction of thrusting (Fig. 1a) (Burchfiel et al., 1992; Burg, 1983). This paradox has inspired a series of deformation models. Early models assumed that the STDS was merging at depth with the Main Central Thrust (MCT), isolating a crustal wedge expulsed upwards (e.g., Burchfiel and Royden, 1985; Burg et al., 1984; England and Molnar, 1993; Grasemann et al., 1999; Grujic et al., 1996; Hodges et al., 1996). Following numerical models analysis, a second class of models considers that the STDS and MCT never merge, but define respectively the top and the bottom of a channel flow of low viscosity lower crust expulsed from beneath the Tibetan plateau (e.g., Beaumont et al., 2001). This last mechanism is often considered to be enhanced by focussed erosion on the Himalayan southern slopes. A third class of model, consider that the STD and the MCT accommodate the southward intrusion of high crystalline series ("tectonic-wedging" of Price, 1986). The main difference with of the crustal wedge models is that the STD and MCT merge southward, and that the STD emerges northward as the Greater Counter Thrust (Webb et al., 2007; Yin, 2006).

Central to all these models are the extent, geometry and kinematics (direction, amount, timing) of the STDS normal faulting, and their relationships with the MCT. Despite numerous studies, the precise timing of initiation and end of the STDS stays controversial has it is often determined indirectly i.e. from the emplacement timing of granites that are interpreted to be genetically linked with the STDS. Here we present a combination of structural, petrographic and geochronologic data that allow us to constrain precisely the timing of the end of STDS normal faulting in the Dinggye area. We then compare this timing with published age elsewhere along the STDS and discuss implications for the Himalayan orogen evolution.

2 The south Tibet detachment system (STDS).

The South Tibetan Detachment system corresponds to a series of north dipping structures accommodating top to the North / normal motion of the Tethyan sedimentary series (TSS) of South Tibet with respect to the underlying High Himalayan crystalline series or Himalayan crystalline slab (HCS) (Fig. 1b) (e.g. Burchfiel et al., 1992; Burg, 1983; Burg et al., 1984). Normal motion has occurred on several ~ parallel low dipping structures that are from top to bottom: a) few brittle normal faults in the TSS, b) a detachment at the contact between the unmetamorphosed TSS and the underlying metamorphic rocks that will be referred here as the STD and c) a ductile shear zone at the top of the HCS, the STD shear zone, where gneisses are highly deformed, lineation trend NE and numerous shear criteria indicate a normal motion (e.g., Burchfiel et al., 1992; Burg et al., 1984; Carosi et al., 1998; Edwards et al., 1996; Searle et al., 1997). The TSS span in age from Ordovician to Eocene and are not metamorphosed, unless for a narrow zone of greenschist metamorphism immediately above the STD, and contact aureoles around the North Himalayan (or South Tibetan) Cenozoic plutons outcropping as a discontinuous belt ~70 km north of the STD (Fig. 1a). The HCS shows a much higher degree of metamorphism. The STDS has been studied along several sections, spanning from Zanskar (~76°E) to the Gonto La (~90°E) (Fig. 1a). The upper HCS series are intruded by numerous large leucogranites plutons and sills, which never crosscut the STD. These granites have been interpreted as having triggered STDS motion (e.g., Burchfiel et al., 1992), or as a consequence of decompression induced by the STDS motion (e.g., Harris et al., 2004). In many cases ages of the leucogranites have been taken as reflecting motion along the STDS. The presence of top to the south structures at the base of the TSS close or within the STD shear zone (e.g., Coleman and Hodges, 1998; Godin et al., 2001; Vannay et al., 2004; Vannay and Hodges, 1996) are generally interpreted has the evidence for Top to the South thrusting on the STDS prior to the onset of top to the North normal faulting (ibid), or by multiple alternation in shear-sense along the STD (Yin, 2006; Webb et al., 2008).

In the Chomolangma area (Fig. 1a and Fig. 2a), two low-angle normal faults, which merge to the north into a unique structure, affect the upper part of the HCS (Carosi et al., 1998; Searle, 1999). The upper fault, the Chomolangma detachment, corresponds to the STD and outcrops just below the summit of the Chomolangma separating the un-metamorphosed Ordovician sedimentary rock above from the North col formation below. The lower Lothse detachment is a ductile shear zone at the top of the HCS. The occurrence of two, possibly diachroneous, superpose low angle normal faults has been reported along other sections of the STDS, for example in the Nar valley east of the Manaslu (Godin et al., 2006a) or in Bhutan (Edwards et al., 1996; Kellett et al., 2009). Some have proposed that the upper STD could still be active east of the Anapurnas in the Takhola graben (Hurtado et al., 2001). Other proposed that there is a major change in the STD kinematics (direction and timing) east of the Yadong graben (Kellett et al., 2009; Wu et al., 1998).

3 Geological setting of the Ama Drime range and surrounding area.

3.1 General structure of the central Himalayas

In the central Himalayas, the main litho-tectonic units define strips, more or less parallel to the range, dipping to the north and separated by major tectonic contacts. The central unit, the Himalayan crystalline slab (HCS) is a sliver of gneiss and granites, sandwiched between less metamorphosed rocks (Fig. 1). To the bottom (South) the HCS rests on the phyllites and quartzites of the Lesser Himalaya (LH, Tumlingtar unit). To the top (North) the HCS is separated from the weakly metamorphosed Tethyan sedimentary series (TSS) by the South Tibetan detachment (STD). South of the Ama Drime range, in the Arun area two main litho-tectonic units can be distinguished within the HCS: the Lower and Upper Himalayan crystalline series (LoHCS and UHCS) (Kali et al., in press). The LoHCS is mostly composed of strongly deformed rocks with metapelites overlying the Num / Ulleri orthogneiss. These latter are bounded at their base by mylonites (Bordet, 1961; Goscombe et al., 2006; Meier and Hiltner, 1993). The basal contact of the LoHCS will be referred here as the lower Main Central Thrust or MCTl (Fig. 1). The UHCS consists mostly of paragneiss, often migmatitic, intruded by Miocene leucogranites (e.g., Borghi et al., 2003). The base of the UHCS also corresponds to a thrust zone: the High Himal Thrust (Goscombe et al., 2006) (MCT of Brunel, 1983; Goscombe and Hand, 2000) that is laterally equivalent of the upper MCT (MCTu, Fig.1; Kali et al., in press).

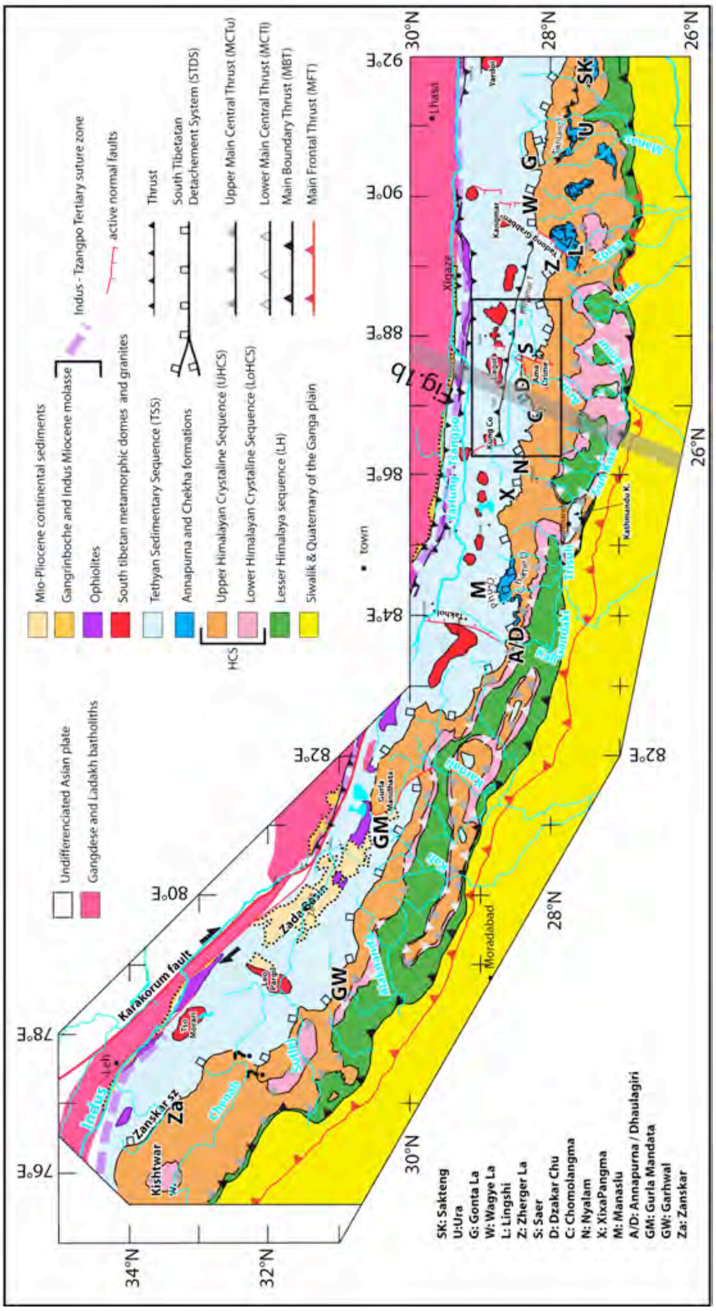

Fig. 1 : Himalayas structural map and cross-section

a) Simplified structural map of the Himalayan range between 76 and 92°E. Black frame corresponds to Fig. 2a map area and grey trace to Fig. 1b cross-section. Bold letters refer to main STDS sites (see Table DR7). An upper and a lower MCT have been distinguished. The trace of the main structures are drawn from local studies (from east to west) by Kellett et al. (2009), Dasgupta et al. (2004), Goscombe et al. (2006), Kali et al. (in press), Searle et al. (1997), Searle and Godin (2003), DeCelles et al. (2004), Vannay et al. (2004), Dèzes et al. (1999).

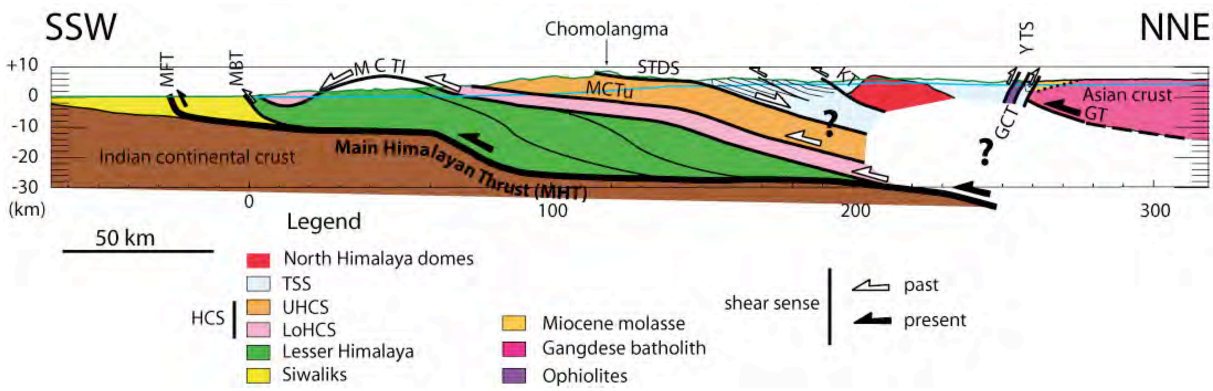

b) Simplified cross section of the Himalayas.
NNE – SSW interpretative cross section at ~87°E, few kilometres west of the Ama Drime range. Main geological units as in Fig. 1a, and main structures geometry from Bollinger et al. (2004). The green line corresponds to the upper relief (i.e., Chomolangma) and the blue line to the lower relief (i.e., Arun valley), no vertical exaggeration. KT, Kangmar thrust; GCT, Great counter thrust; GT, Gangdese Thrust;YTS, Yarlung-Tsangpo suture zone

3.2 The Ama Drime range

The Ama Drime range is a N-S crest culminating at 6730m *a.s.l.* (Nyonni Ri), protruding north of the main stretch of the Himalaya between the Kanchengjunga (8586m) and the Chomolangma/Everest (8848m) (Fig. 1a and Fig. 2a).

The Ama Drime range is a horst bounded on both sides by N-S active faults at the southern end of the Xainza-Dinggye fault system (e.g., Armijo et al., 1986). Recent activity of the Kharta fault to the west and Dinggye fault to the east are attested by spectacular triangular facets, brittle fault planes, and cataclasites (e.g., Armijo et al., 1986; Holland et al., 1998; Kali et al., in press; Zhang and Guo, 2007). On the eastern side of the range, normal faults parallel to the Dinggye fault slice the foothills to at least 5 km away from the topographic front and have tilted to the west the metamorphic series of the STD shear zone (Burchfiel et al., 1992) (Fig. 2c). Age versus elevation relationship of (U-Th)/He apatite from the Ama Drime suggests exhumation rate of ~1mm/yr between ~4 and 1.5 Ma (Jessup et al., 2008b; Kali et al., in press).

Most rocks comprised between the Kharta and Dinggye active faults are migmatitic orthogneiss containing large layers and boudins of metabasites that have recorded eclogite facies metamorphism, (Cottle et al., 2009; Groppo et al., 2007; Kali et al., in press; Lombardo and Rolfo, 2000). These rocks have been designated as the Ama Drime orthogneissic unit (ADO, Fig. 2a) and attributed to the LoHCS (Kali et al., in press) (Fig. 2a). Paragneiss containing rare amphibolites and intruded by numerous leucogranites in the northern part of the Ama Drime outcrop. These rocks define the Ama Drime paragneissic unit (ADP) that very probably belongs to the UHCS (Kali et al., in press) (Fig. 2).

On both flank of the Ama Drime, in the immediate footwall of the active normal faults, the HCS rocks are affected by pervasive normal ductile deformation in the Kharta and Dinggye shear zones (Burchfiel et al., 1992; Jessup et al., 2008b; Kali et al., in press; Zhang and Guo, 2007).

3.3 The STDS in the Dinggye – Kharta area.

Near the Ama Drime range, the STD has been described across the Dzakar river (Burg et al., 1984; Cottle et al., 2009; Cottle et al., 2007) (stars 2 and 3, Fig. 2a), and south of Dinggye near Saer (Burchfiel et al., 1992) (star 1, Fig. 2a). The STD separates deformed micaschist of the HCS containing leucogranites pods below, from weakly metamorphosed Tethyan sedimentary series above. Combining published observations, our own field work, and Landsat satellite image interpretation, we propose a map of the STD (Fig. 2a, b). This mapping confirms that the STD is deflected to the north around the Ama Drime range, and is cut and offset by the N-S normal faults and shear zones (Burchfiel et al., 1992; Jessup et al., 2008b; Kali et al., in press; Zhang and Guo, 2007). Kali et al. (in press) estimate that the apparent vertical offsets of the STD are 4.4 to 9.4 km and 1.3 to 4 km along the Dinggye and Sangkar faults respectively.

Below the detachment, in the STD shear zone (STD sz), high temperature deformation affecting both the micashists and the leucogranites is characterized by ~E-W foliations dipping to the north, NE trending lineation and top to the north sense of shear (Fig. 3 Fig. 4a).

Near Dinggye, the STD dips ~10±5° to the NNE. Because they have been tilted by late N-S normal faults, foliations locally dip to the NW (~45° on average), but lineation constantly trend NE (Table DR1, Fig. 2c, Fig. 3f). Where not affected by late normal faults the micaschist are almost horizontal and the lineation trends NNE (Fig. 3d; Fig. 3f). If foliations tilted in between the late normal faults, are rotated back to nearly horizontal, the corresponding lineation trend N25 in good agreement with the not tilted ones (Fig. 3g).

4 P-T-t-D path in the STD shear zone near Dinggye.

South of Dinggye, ~100m below the STD (outcrop 05-222, N28°11’4.5’’ E87°46’51.4’’), garnet micashists (sample T5D19) and leucogranites (sample T5D20) are deformed together showing top to the NE shear sense. Few undeformed leucogranites (sample T5D21) crosscut the deformed leucogranites and micaschist (Table DR2, Fig. 2c; Fig. 3). Conjoint petrographic, chemical and geochronological analysis of these samples yields constraints on the P-T-D-t path of the STD shear zone.

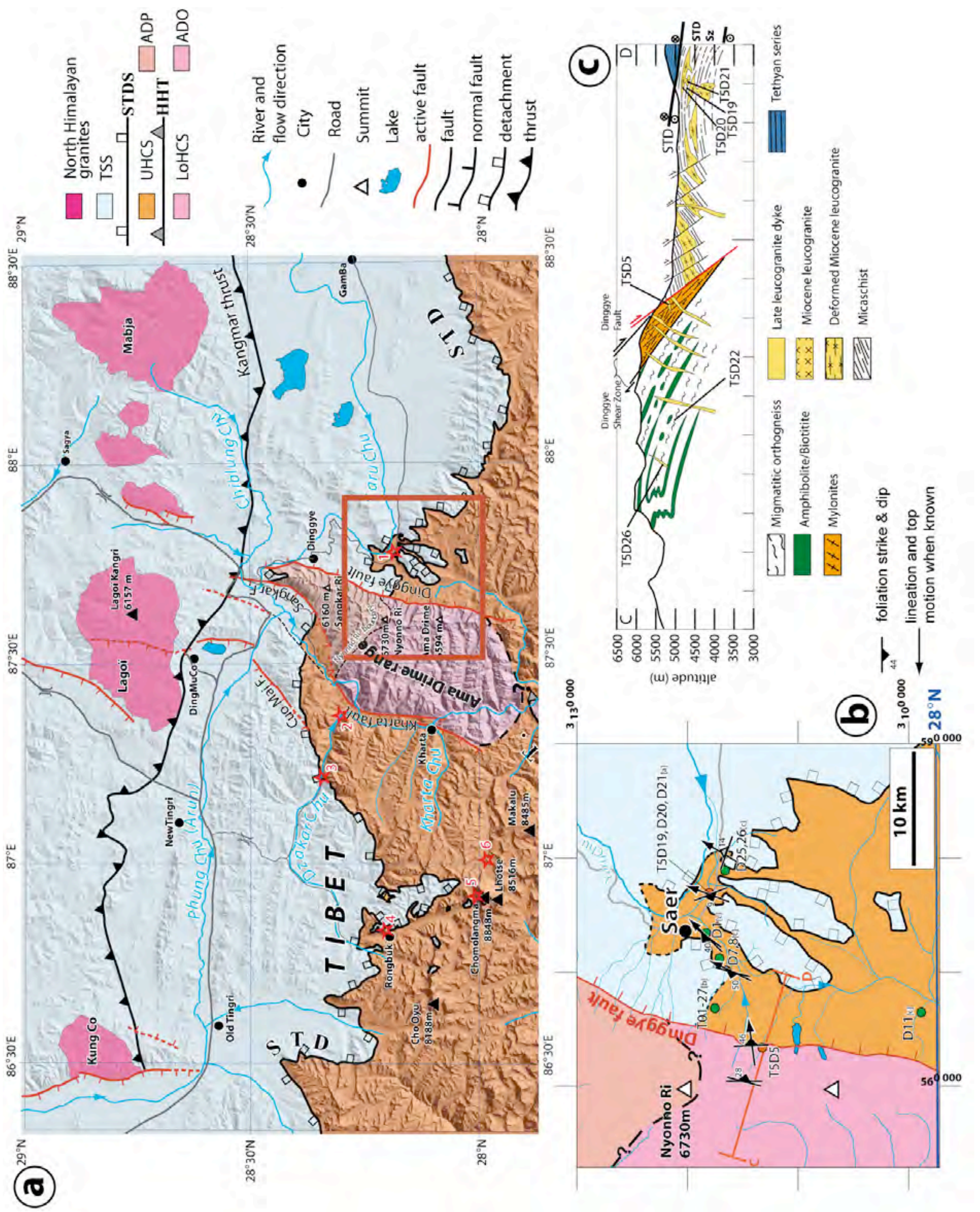

Fig. 2 : Structural frame of the studied area and samples location.

a) Structural map of the STD system in the Chomolangma-Dinggye area.

Drawn from previous works, satellite image interpretation and fieldwork. Red frame indicates Fig. 2b. Projection is UTM45. Stars locate main outcrop discussed in text: 1 05-222; 2 Thongmön, 3 Dzakar Chu section, 4: Rongbuk monastery, 5: Chomolangma yellow band, 6: Kangshung.

b) Structural map of the Saer area. Same legend as Fig. 2a. Samples from this study [a], Zhang and Guo (2007) [b] and Hodges et al. (1994) [c] are located as well as section C-D (see Fig. 2c)

c) Geological cross section of the eastern flank of the Ama Drime range south of Dinggye. See Fig. 2b for location**.**

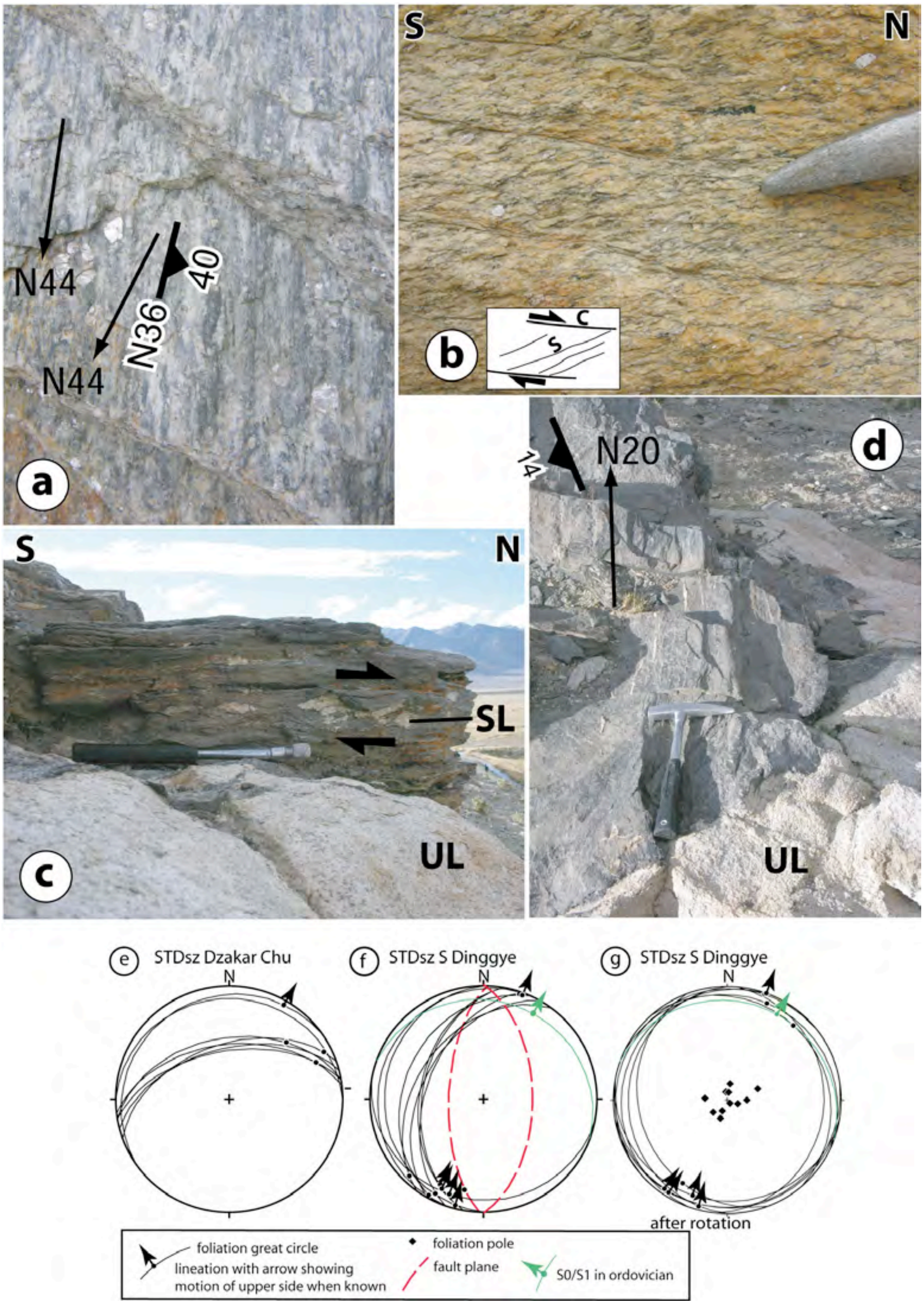

.

Fig. 3 Deformation characters of micaschist and leucogranites of the STD shear zone

a to d picture of outcrop 05-222, located south of Dinggye ~100 meters below the STD. See Fig. 2b for location. **a)** Mylonitic leucogranites. Lineation is cross-cut by a tourmaline bearing dyke. Oblique view from above. Hammer gives Scale. **b)** C-S criteria indicating top the North shearing in mylonitic leucogranites (see Fig. 3a). Hammer gives Scale. **c)** Flat lying micaschist (sample T5D19) with sheared levels of mylonitic leucogranite (SL, sample T5D21), intruded by undeformed leucogranite pod (UL, sample T5D20). Hammer gives Scale. View towards W. **d)** Undeformed leucogranite pod crosscuting micaschist with N20 trending lineation. View from above. Hammer gives Scale. See also Fig. 3c. **e to g**: Foliation and lineation attitude. Lower hemisphere Schmidt projection. Arrows indicate hanging wall shear direction when known. **e)** Foliations and lineations in the STD shear zone in the Dzakar Chu valley (star 2, Fig. 2a). **f)** Foliations and lineations in the STD shear zone south of Dingye. Outcrop 05-222 (star 1, Fig. 2a), and neighbouring outcrops. The green symbols correspond to deformation in the Ordovician sandstones. The red dashed lines are late brittle faults. **g)** Same as f but with foliations affected by tilting near late ~N-S faults, rotated back to nearly horizontal. Rotation axis: N18° 0°, angle: 45.5°. After rotation average lineation trends N 26°

4.1 Micaschist P-T evolution.

T5D19 micaschist contain quartz, plagioclase, biotite, sillimanite, staurolite, garnet, tourmaline and rare white micas. The foliation is defined by preferential orientation of biotites and the lineation by sillimanites. This foliation surrounds aggregates containing garnet with oxides and quartz inclusions, staurolite, plagioclase, biotite and quartz relicts (Fig. 4a). Garnet also occurs outside of the aggregates, as porphyroblasts showing asymmetric biotite-sillimanite tails (Fig. 4a). Biotite and quartz inclusions within these garnets define a relict foliation oblique to the matrix one. C-S relations associated with biotite and sillimanite crystallization show top to the north high temperature normal movement (Fig. 4a).

Two successive paragenesis are recognised:

(1) Garnet + staurolite + biotite + quartz + plagioclase in aggregates and in the garnet porphyroblasts cores.

(2) Garnet porphyroblasts + biotite + sillimanite + quartz + plagioclase in the matrix.

Biotites in inclusions within garnet are slightly more Fe-rich than those within the foliation (X_{Fe} 0.72-0.67 and 0.63-0.65 respectively) (Table DR3). Plagioclases from the two paragenesis have similar albitic composition (X_{ab} 0.88-0.89). Staurolite has a high FeO (14.6 wt%) and low MgO (0.9 wt%) (Table DR3). Garnet from the aggregates and within the foliation presents the same chemical zoning. Cartographies and profiles show a simple chemical zonation characterized, from core (zone I) to rim (zone II), by almandine and pyrope increase (86 to 89 % and 7.5 to 9.5 % respectively) and grossular decrease (6.2 to 2.1 %) (Table DR3, Fig. 4b, c). Such chemical zoning is typical of garnet growth during prograde metamorphism in greenschist and amphibolite facies rocks (Spear, 1993).

Mineral assemblage of the studied metapelites can be described in the NCKFMASH system (Spear, 1993). Perple_X'07 has been used for the calculation of pseudosections in the NCKFMASH system using the 2004 revised version of the internally consistent thermodynamic dataset of Holland & Powell (Holland and Powell, 1998). In the calculation H_2O was considered as a saturated phase and quartz as in excess. Whole rock composition and detailed methodology are given in appendix I.

According to the pseudosection and garnet isopleths, garnet core composition corresponds to P-T conditions of ~0.6 GPa and ~550°C (Zone I Fig. 4d), and the rim to slightly lower P and higher T (0.5 GPa and 625°C, zone II). Rim temperature was also constrained applying a cationic exchange garnet-biotite thermometer using the Holdaway (Holdaway, 2000) 5AV calibration. Biotite and garnet II pair in close contact give T of 650+/-50°C assuming a pressure of 0.4 to 0.6 GPa. One pair implying a biotite inclusion and a garnet with composition intermediate between I and II give slightly lower T of 590°C+/-10°C for the same P range. Altogether, pseudosection calculation as well as classical thermometry thus suggest a 100 to 150°C heating episode and a slight decompression (~0.1 GPa) between the garnet core and rim. PT path during the final exhumation is only constrained by the absence of cordierite in thin section (Fig. 4d).

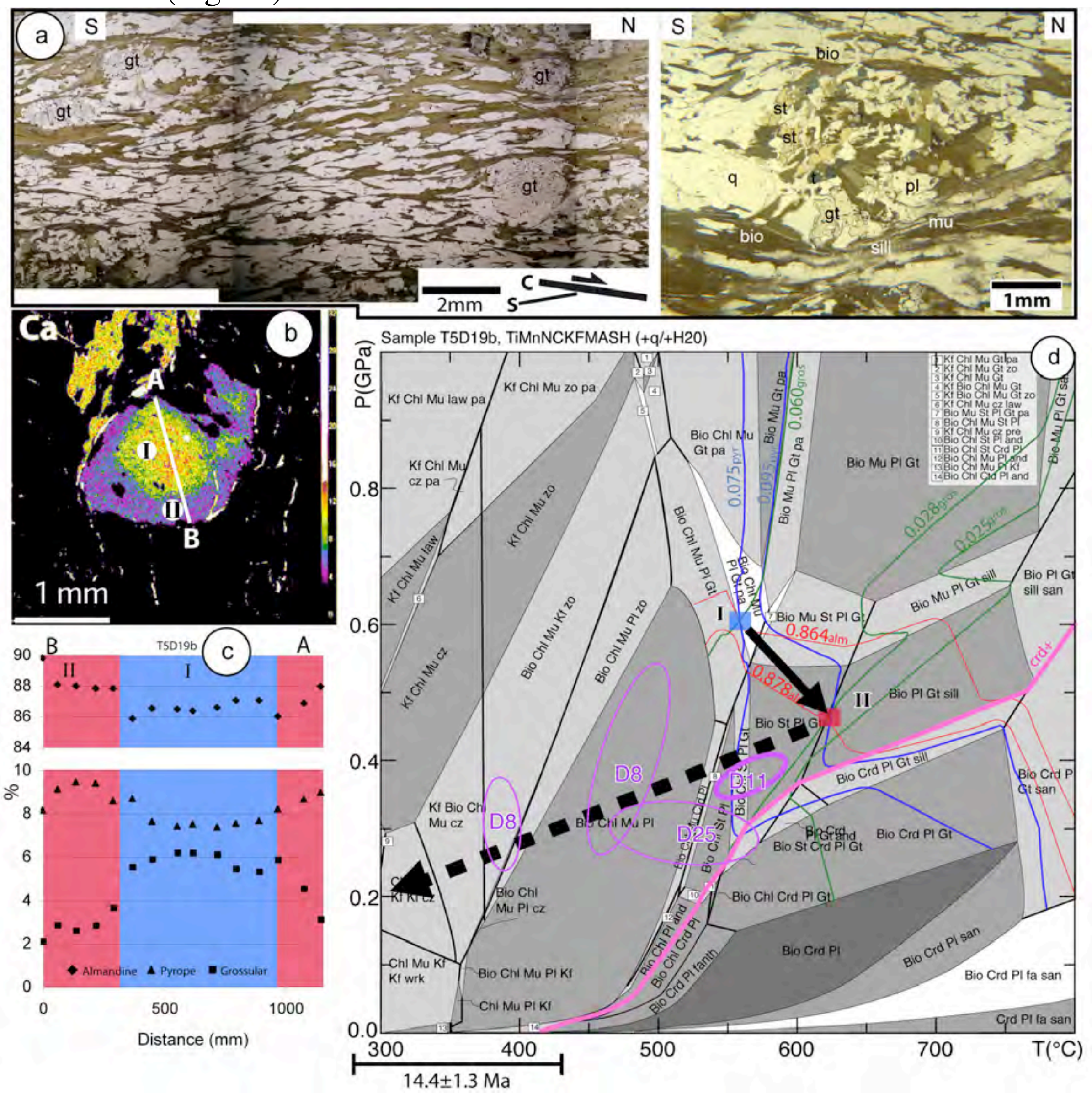

Fig. 4 : PT path in the STD Shear Zone (sample T5D19).

a) T5D19 thin section pictures. Section cut parallel to lineation and perpendicular to foliation, natural light. Left: garnets in the foliation (S) and north dipping shear planes (C). Right: garnet, staurolite, plagioclase, biotite and quartz aggregate. Biotite and sillimanite underline the foliation and the shear planes. **b)** Ca-X-ray map and **c)** composition profile A-B showing chemical zoning of garnet (Table DR3). **d)** NCKFMASH pseudosection (Perple_X2007) for the measured whole-rock composition (appendix I). White, light grey, medium grey and dark grey fields are di-, tri-, quadri- and quinivariant fields respectively. Mineral abbreviations follow Holland and Powell (1998). Green, red and blue lines respectively corresponds to grossular, almandine, and pyrope isopleths. Zone I corresponds to the garnet core and zone II to the garnet rim. The purple ellipses indicate P-T estimates of Hodges et al. (1994) using the garnet-biotite thermometer (1978). The 14.4 ± 1.3 Ma age corresponds to the average of all Ar/Ar micas ages (this work, Hodges et al. 1992; Zhang & Guo, 2007). The associate temperature (black heavy line) is based on the range of closure temperatures for biotites and muscovites (Hames and Bowring, 1994; Harrison et al., 1985).

Using cationic exchange Garnet-biotite thermobarometry (Hodges et al., 1994) provided P-T estimates for nearby UHCS micaschist (samples D8, D11 and D25 located on Fig. 2b). Sample D11 with similar mineralogy than T5D19b yields slightly lower pressure and temperature (0.4 GPa and 590°C) than our estimate for garnet rims (Fig. 4d). Sillimanite-absent D8 and D25 samples yield lower temperatures (375-550°C) (Fig. 4d). Given the large number of leucogranites, the whole Dinggye-Kharta series was heated at the time of intrusion, and it is improbable that the offset in temperature results from a local heating event that would have affected T5D19 but not Hodges's et al. samples. The observed temperature variations observed near Dinggye could result from varying distances to the STD if, as in the Everest and Zanskar, the peak pressure and temperature increase with structural depth below the STD (Dezes et al., 1999; Jessup et al., 2008a). However, if D8 and D25 appear to have been sampled closer from the STD than T5D19, the structural depth of D11 is unconstrained as the STD has been eroded away in that area (Fig. 2b). Another possibility is that the temperature difference results from methodological uncertainties.

That P-T path documents a phase of slight decompression during heating from 0.6 to 0.5 GPa (from 18 to 22 km depth), followed by a phase of decompression and cooling (Fig. 4d). A first foliation that is now visible in inclusion within most garnets developed at the time of heating. S-C structures developed during top to the north shearing in high-temperature conditions (garnet rims and sillimanite).

4.2 Geochronology.

Single monazites and zircons were analysed with high resolution ion microprobes, respectively the SHRIMP II at the Institute of Geology of Beijing, China, and the Cameca IMS 1270 at CRPG in Nancy, France. The Argon spectrometric analysis where conducted during furnace step heating at the university Montpellier2, France. Analytical conditions are given in appendix II.

4.2.1 U/Pb results

Zircons in both the undeformed (T5D21) and the deformed (T5D20) granites are mostly clear and euhedral in shape, elongated to sometimes acicular (Fig. 5e,f). Rare stocky grains are also found. Blurred cores are found in most zircons whether they are elongated or not. On a concordia plot, both sample show approximately the same age distribution regardless of the location (cores/rim) of the analysis, with a large Paleozoic to Neoproterozoic (300-900 Ma) inheritance, two even older discordant analyses (>1 Ga), and few Cenozoic ages (Fig. 5a, Table DR4).

In T5D21 (undeformed) seven spots from 4 different crystals including 5 borders and two cores, yield apparent Miocene ages (Fig. 5b, Table DR4-1). All measurements, unless one core (Fig. 5f), from these 4 crystals correspond to young ages and thus suggest zircon neocrystallisation with limited, or undetectable, overgrowth on inherited zircons within the melt.

Two of these data plot slightly above the concordia probably due to excessive common lead correction. The other data correspond to a discordia with a lower intercept at 13.0 ± 2.2 Ma and an upper intercept at 729 ± 290 Ma (MSWD = 0.9) (Fig. 5b). The ^{206}Pb / ^{238}U average age of the five nearly concordant data is 13.6 ± 1.3 Ma (Fig. 5c) in agreement with the lower intercept of the discordia. A regression in the Tera-Wasserburg diagram forced through present day common lead yields, using the same five points, a similar age within errors (13.7±1.3 Ma, MSWD=4.8) (Fig. 5d).

In sample T5D20 (deformed) only three spots yield apparent Miocene ages with ^{238}U/^{206}Pb ages between 14.2±0.4 Ma and 43.3±1.7 Ma respectively (TableDR4-2). The youngest of these data corresponds to the tip of a zircon whose core yields a much older age (Fig. 5e). The young age is slightly discordant however (Fig. 5b) and cannot be used to constrain precisely the time of zircon overgrowth.

Monazites from both granites are 100 μm on average, euhedral and have a homogeneous unzoned texture. Grains with obvious zircon or U-rich minerals inclusions were avoided using CL images (Fig. 5k,l). Ages are indistinguishable within errors between cores and rims of each grain (Table DR5). Overall, monazites populations from both the deformed and undeformed granite yield Miocene ^{208}Pb/^{232}Th ages corrected for common lead via ^{204}Pb analysis.

T5D20 shows fairly homogeneous ^{208}Pb/^{232}Th ages (15.1-16.5 Ma) if one excludes two outliers at ca 19.5 Ma (Fig. 5g). The average of the 11 younger data is 15.99±0.30 Ma (MSWD=0.9), (Table DR5-1, Fig. 5g). Using a Tera-Wasserburg diagram, regression forced though present day common lead gives an age of 16.87±0.28 Ma (9 points, MSWD=1.08) excluding 4 points, two of which being the outliers at ca 19.5 Ma (Fig. 5h).

Figure 5 : T5D20 and T5D21 U/Pb results.

a to f : zircons**, g to l** : monazite. Corresponding data are summarized in Table 1, and listed in Table DR4 for zircons and Table DR5 for monazites. Concordia lines appear in grey. Probe spot names appear as sample/crystal-spot location. 6/8 and 7/5 refer to the ^{206}Pb/^{238}U and ^{207}Pb/^{235}U ages respectively. **a)** ^{206}Pb/^{238}U versus ^{207}Pb/^{235}U concordia plot for T5D21 and T5D20 zircons. Error ellipse (2 sigma) plotted only when larger than square symbol. Younger ages detailed in b). **b)** Cenozoic part of the ^{206}Pb/^{238}U versus ^{207}Pb/^{235}U concordia plot for T5D21 and T5D20 zircons. **c)** Cenozoic ^{206}Pb/^{238}U ages of T5D21 zircons. An average of 13.6±1.3 Ma is calculated (see text for details). **d)** T5D20 and T5D21 zircons Tera-Wasserburg diagram, with regression forced through present day common lead for T5D21. **e)** Natural light (left) and cathodo-luminescence (right) images of sample T5D20 zircon crystal n° 28 with ion probe spots and corresponding ages. **f)** Natural light picture of sample T5D21 zircon crystal n° 3 with ion probe spots and corresponding ages. **g)** T5D21 and T5D20 monazites ^{208}Pb/^{232}Th ages with proposed average ages. **h)** T5D20 and T5D21 monazite Tera-Wasserburg diagram, with regressions forced through present day common lead. Two populations are distinguished for T5D21. **i)** Cumulative probability plot of ^{208}Pb/^{232}Th T5D21 monazite ages. The asymmetric shape of the plot suggests two populations, see text for details. **j)** Cumulative probability plot of ^{208}Pb/^{232}Th T5D21 monazite age for each of the two populations. **k)** Examples of optical (left) and Cathodo-luminescence (right) images of T5D20 monazites with corresponding ages. **l)** Example of optical (left) and Cathodo-luminescence (right) images of T5D21 monazite with corresponding ages.

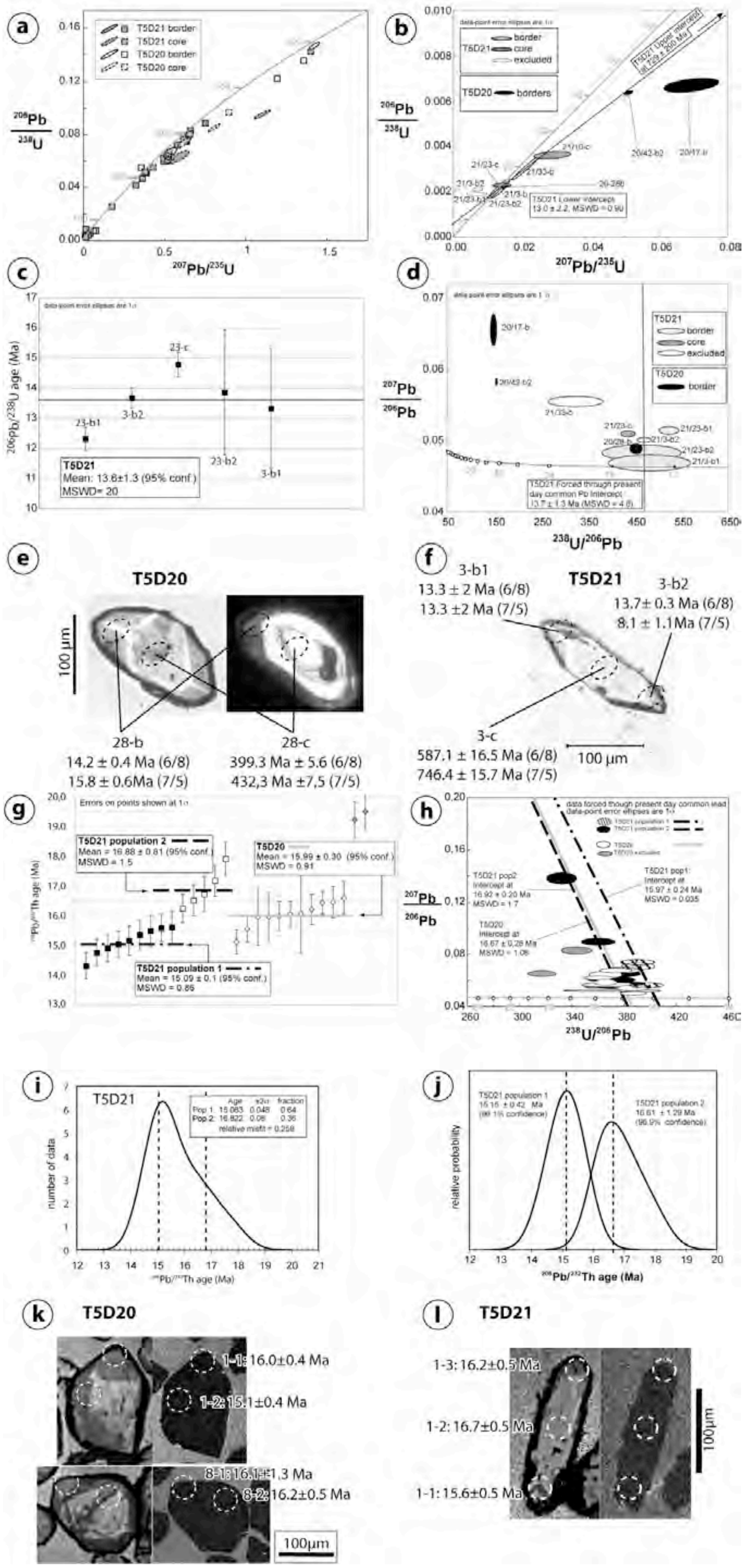

T5D21 shows a larger $^{208}Pb/^{232}Th$ age range (14.3-17.9 Ma, Table DR5-2) and a significant asymmetry of the age probability plot suggests that two populations are present, with one dominant population around 15Ma hiding an older one (Fig. 5i). Age histogram deconvolution using isoplot software (Ludwig, 2003) leads two central ages at 15.06±0.05 Ma and 16.82±0.08 Ma (Fig; 5i), each population having a Gaussian age distribution (Fig. 5j). These ages are almost identical to the weighted averages obtained on two splits of the population below and above 16 Ma: 15.09±0.31 Ma (MSWD=0.86) for population 1, and 16.88±0.81 Ma (MSWD=1.5) population 2 (Fig. 5g). Ages and populations do not correlate in any way with spot analysis locations nor other features from the monazites analyzed. In the Tera-Wasserburg plot, data corresponding to the 3 youngest ^{204}Pb corrected ages are aligned and yield an age of 15.97± 0.24 Ma (MSWD=0.035), while all other data point to 16.92±0.20 Ma (MSWD=1.7) (Fig. 5h)All monazite and zircon U/Pb ages described above span between ~12 and ~20 Ma confirming a Miocene age for the leucogranites within the STD shear zone (Table 1). In each given sample monazites tend to be older than the youngest zircons which is rather unusual. The fact that monazites show a relatively large $^{208}Pb/^{232}Th$ age range and that sub-populations are distinguished whatever the way to analyse the data, suggests that favourable conditions for crystallization monazites have been maintained for some Myrs in both samples while granites were still partly above solidus and thus probably mobile. The age of the youngest monazite population should correspond to the final crystallization of the granite. If one considers the $^{208}Pb/^{232}Th$ monazite age this would be 15.99±0.30 Ma for T5D20 (deformed) and 15.09±0.11 Ma for T5D21 (undeformed). The Tera-Wasserburg approach yields ~1Myr older ages: 16.87±0.28 Ma (T5D20) and 15.97±0.24 (T5D21). In both case, the deformed granite is ~ 1 Myr older than the cross-cutting one.

The youngest zircons are 13.6±1.3 Ma old in T5D21. This age is identical within 1σ errors with that of the $^{208}Pb/^{232}Th$ age of Monazites population 1 (15.09±0.11), confirming that this latter age is probably the best estimate for the granite crystallization. The deformed granite (T5D20) most probably emplaced at ~16 Ma within the deforming STD series, while T5D21 emplaced at ~15Ma, sealing deformation in the STD shear zone at this location

4.2.2 Ar/Ar results

Biotites from T5D19 micaschist yield an irregular age spectra, and a weighted average age of 15.2 ± 0.3 Ma for 6 out of the 11 steps corresponding to 88% of the ^{39}Ar released (Fig. 6c, Table 2, Table DR6-1). This age is similar within errors to the age of the 1000°C and 1050°C steps which account for 47% of the ^{39}Ar released (Fig. 6c, Table DR6-1), and to the inverse isochrone age (Fig. 6b, Table 2). Although this cannot be considered as meaningful as a true plateau age, the 15.2 ± 0.3 Ma appears robust.

Section/site	Sample			Average 206/238 age for zircon and 208/232 age for monazite				Inverse isochron (Tera Wasserburg) 207/206 vs 238/206					Concordia 206/238 vs 207/2356				
	Number	rock type	Mineral type	Age, Ma	MSWD	Number of spots	Spots	Age, Ma	Upper Intercept	MSWD	Number of spots	Spots	Age, Ma	Upper Intercept, Ma	MSWD	Number of spots	Spots
STDS shear zone	T5D21	undeformed leucogranite	Zircon	13.6 ± 1.3	20	5	40,2,3b2b 23b2b3,39	13.7 ± 1.3	Common lead	4.8	5	40,2,3b2b 23b2b3,39	13.3 ± 2.0	729 ± 290	0,9	5	3b2b,23b2b3 39,33b1b1,13
			Monazite	15.1 ± 0.1	0.9	9	7.1,6.1,8.1,12.1,9.1 10.1,7.2,4.1,1.1	16.0 ± 0.2	Common lead	0.04	3	7.1,6.1,8.1					
				16.9 ± 0.8	1.5	5	1.3,11.1,1.2,3.1,5.1	16.9 ± 0.2	Common lead	1.7	11	12.1,9.1,10.1,7.2, 4.1,1.1 1.3,11.1,1.2,3.1,5.1					
				15.6 ± 0.6	16	14	all spots										
	T5D20	deformed leucogranite	zircon	14.2±0.4		1	15										
			Monazite	16.0 ± 0.3	0.9	11	1.2,9.1,15.1,9.2,10.1,1.1 8.2,8.1,4.1,14.1,13.1	16.9 ± 0.3	Common lead	1.1	9	1.2,9.1,15.1,9.2 10.1,1.1,8.2,8.1,4.1					

Table 1 :U/Pb data summary.
For samples location see Table DR2 and Fig. 2b. Data plotted on Fig.6. Detailed data are given in Table DR4 and Table DR5.

Muscovites from the deformed granitic lenses (T5D20) within the micaschist show a saddle-shape age spectra suggesting a maximum age of 13.9 ± 0.2 Ma. The corresponding inverse isochron gives an age of 13.6 ± 0.5 Ma (Fig. 6a,b; Table 2; Table DR6-2). Biotites from the same sample are slightly older with a weighted mean average age of 14.2 ± 0.1 Ma similar within errors to the isochron age (14.5±0.2 Ma) (Fig. 6a,b; Table 2, Table DR6-1).

Muscovite from the undeformed granite sample T5D21 displays a plateau, slightly saddle-shaped, with a weighted average age of 13.8 ± 0.2 Ma almost undistinguishable from the isochron age of 13.6 ± 0.2 Ma indicating a slight excess argon (Fig. 6c,d; Table 2, Table DR6-2).

Such results are in agreement with previous argon dating in the same area. Hodges et al. (1994) collected samples from the STD shear zone south of Dinggye (samples D1, 7, 8, 25, and 26 located on Fig. 2a). Argon dating of muscovites yields ages between 12.8 and 14.9 Ma while biotites are from 14.5 to 15.7 Ma. These data are also in agreement with the muscovite age of 14.2 ± 0.5 Ma found by Zhang and Guo (Zhang and Guo, 2007) for a mylonitic leucogranite within the STD shear zone (sample T01- 27 Fig. 2a).

Overall, biotites and muscovites of the STD shear zone have essentially the same weight mean ages: 14.4 ± 1.3 for biotites and 14.0 ± 0.5 for muscovites (Table 2). This suggests very rapid cooling from 405±35°C (clossure temperature for muscovite calculated for cooling rates between 1 and 100°C/Ma using the diffusion parameters at ~5kb given by Harrison et al., 2009) to 320±40°C (closure temperature for biotites, e.g. Harrison et al., 1985) in the 14.4±1.3 (weight mean age of all available mica ages with 2σ error) time interval.

Section/site	Sample				Plateau Age			Inverse Isochron Age				Total Fusion Age
	Number	rock type	Altitude	Mineral type		Age, Ma	Steps	Age, Ma	$^{40}Ar/^{36}Ar_i$	MSWD	Steps	Age, Ma
STDS shear zone	T5D19b	garnet-sillimanite micaschist	4263	biotite	SMA	15.2 ± 0.3	2 steps/11 (7-8) 50% of gas	15.8 ± 0.8	302 ± 19	10.7	6 steps/11 (4-9) 90% of gas	16.3 ± 0.2
	T5D20	deformed leucogranite	4263	biotite	SMA	14.2 ± 0.1	4 steps/12 (7-8) 80% of gas	14.5 ± 0.2	295 ± 9	5.4	6 steps/12 (4-11) 50% of gas	13.9 ± 0.1
				muscovite				13.6 ± 0.5	349 ± 20	7.6	7 steps/12 (4-6, 8-11) 90% of gas	13.9 ± 0.2
	T5D21	undeformed leucogranite	4263	muscovite	WMP	13.8 ±0.2	9 steps/14 (5-13) 95% of gas	13.6 ± 0.2	321 ± 4	1.4	11 steps/14 (3, 5-14) 90% of gas	14.2 ± 0.1

Table 2 :Ar/Ar data summary.
See Fig. 6. Detailed data are given in Table DR6

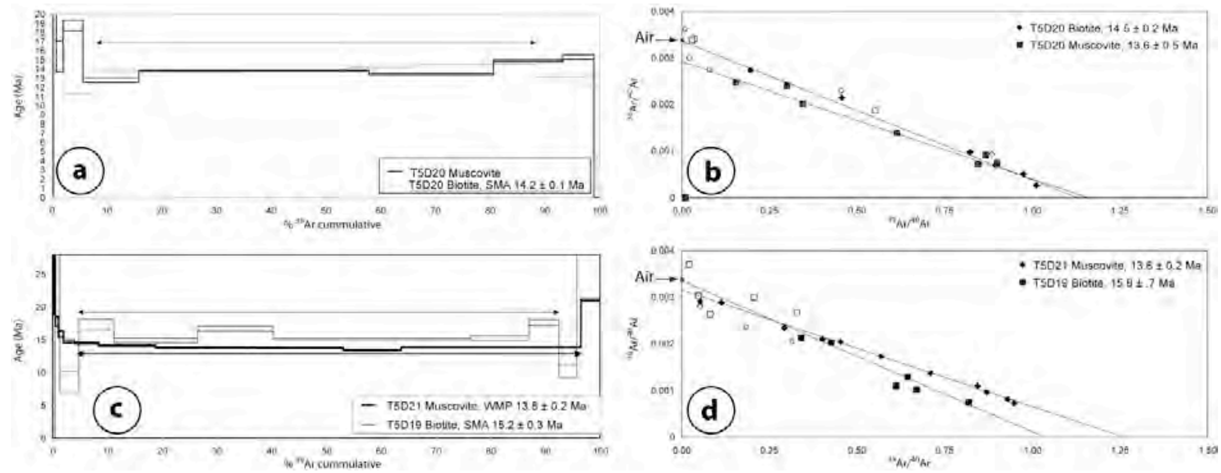

Figure 6 : Argon data
Corresponding data are summarized in Table 2 and listed in Table DR6. For age spectrum the double arrows indicate the steps used in age calculation. For inverse isochrone plots empty symbols not used in age calculation.
a) *T5D20 muscovite and biotite age spectra.* ***b)*** *T5D20 muscovite and biotite inverse isochrone plot.* ***c)*** *T5D21 muscovite and T5D19 biotite age spectra.* ***d)*** *T5D21 muscovite and T5D19 biotite inverse isochrone plot.*

5 Discussion: timing of the STD in the Ama Drime area, comparison with other locations.

5.1 P-T-t-D and timing of end of motion in STDS near Dinggye.

When combining the data presented above for outcrop 05-222, the picture that emerges, is that of an STD shear zone with top to the NE ductile shearing starting at a depth of ~22 km after heating to ~650°C and leucogranite emplacement. Locally ductile deformation stopped at ~15 Ma. Argon data indicate that the following cooling was fast and lasted until at least ~13.6 Ma, suggesting that deformation pursued for at least ~1 Ma, within the STDsz, and / or on brittle structures above outcrop 05-222. Such fast cooling could also be related with fast erosion rather than tectonic denudation. However, the occurrence of nearly un-metamorphosed TSS rocks just above the STD, locally observed as klippen (Burchfiel et al., 1992; Hodges et al., 1994; this study) (Fig. 2b) implies that the total amount of erosion in the area was relatively small and favour the interpretation of a rapid cooling linked to normal faulting.

In the absence of granites crosscutting all structures or low temperature geochronologic data it is difficult to pin down the age of the last down to the North motion. However, as mentioned above, the STDS is cut and offset by the Dinggye N-S active fault and shear zone that correspond to an E-W direction of extension, almost perpendicular to that of the STDS (NNE-SSW). The initiation age of the Dinggye fault will thus provide a minimum age for the end of motion on the STDS near Dinggye.

(U-Th)/He apatite ages within the AmaDrime range suggest exhumation at a rate of ~1mm/yr since at least ~4Ma, and thus that the Dinggye active normal fault is active since at least that time (Jessup et al., 2008b; Kali et al., in press). Kali et al. (in press) also report a leucocratic dyke that cross-cuts the ductile deformation fabric in the footwall of the Dinggye normal fault. Monazites from that dyke show two $^{208}Pb/^{232}Th$ ages populations at 13.09±0.32 Ma and 10.98±0.39 Ma, the youngest one being interpreted at the timing of crystallisation. This implies that down to the east ductile normal faulting was, at least locally, over at ~11 Ma, but rapid normal faulting pursued, as micas argon ages suggest a rapid cooling in the 13.7 –10.2 Ma time interval (Kali et al., in press). It follows that any motion on the STDS ended prior to ~11 Ma, time at which down to the west motion on the Dinggye N-S shear zone had already occurred. It can thus be concluded that motion on the STDS near Dinggye ended between 13.6 and 11 Ma.

5.2. Amount of exhumation at the time of STDS activity.

T5D19 exhumation (~0.6 GPa, ~22 km) occurred since the onset of the STDS, with motion absorbed both within the STD shear zone structurally above outcrop 05-222, and along the STD. Combining PT path and cooling ages (Fig. 4d) it appears that the exhumation of the STDsz rocks since 14.1±0.5 Ma, time at which they cooled down to ~320°C, is less than 0.4 GPa (paragenesis II ≥600°C, Fig.4). Taking into account Hodges et al. (1992) P-T estimates reduces this value to less than 0.3 GPa (Fig. 4). The amount of exhumation linked with the STDS is thus comprised between ≥ 0.3 Gpa (~11km) and ≤0.6 Gpa (~22km), which would correspond to between ≥64 and ≤128 km of slip assuming simple shear and a regular dip of 10° for the STD. For a STD dip of 15° or 5°, the slip range would be 42-85 km and 128-255 km respectively. As a pure shear component of deformation (vertical flattening) appears widespread in the UHCS rocks below the STD (Law et al., 2004), the amount of throw, and thus of slip, corresponding to a given exhumation is probably overestimated.

Previous estimates for STDS slip in other localities range between more than 15 (W on Fig. 1a), (Edwards et al., 1996) to more than 140km (SK on Fig. 1a), (Grujic et al., 2002). Estimates for the Dzakar Chu (D) section, the closest from our study area vary between 50 and 120 km depending on the dip assumed for the STDsz (Cottle et al., 2007). From the available data it appears difficult to get a precise amount of motion on the STDS (see also Yin, 2006), and thus to use this parameter in the discussion on the mechanics of the Himalayas collision zone.

5.3 Timing of the STDS: along strike diachronism?

Several authors have proposed that the STDS and MCT slips where coeval (see Yin, 2006 for a review). However few authors have systematically investigated the STDS timing along strike of the Himalayas. From a compilation of previous studies (Godin et al., 2006b) define an upper and a lower STD. For each structure (Godin et al., 2006b) estimate a “best-fit age” corresponding to the age at which the fault was active everywhere along strike. These “best-fit ages" are of ~21 Ma for the upper STD and ~18 Ma for the lower one (Fig. 7). The authors also infer that the lower STD was mostly active between 24 and 12 Ma with the upper STD apparently starting latter and lasting longer between 19 and perhaps 0 Ma. That study is however lacking any critical analysis of the data set, and of the diachronism of motion between the various localities along strike that these data seems to imply. We discuss below in more detail the issue of the timing of the end of motion along the STDS and its diachronism / synchronism along strike.

The STD has no clear morphological expression, it is crosscut by the active N-S normal faults (Gurla Mandata, Thakhola, Ama Drime, Yadong) and no crustal earthquake indicative of ~E-W normal faulting has ever been documented in the South Tibetan crust. The STD is thus a fossil structure.

Most published studies that allow inferring an age for the end of motion on the STDS are listed in appendix III, and are summarised in Table DR7. Probably based on the idea that melting was linked to normal shear on the STDS, several studies rest on the youngest ages of the leucogranites affected by the STDS, to estimate the age of cessation of normal faulting (squares, Fig. 7). Such analysis yields 22-16 Ma ages along most of the belt, with younger (~12 Ma) ages East of the Yadong active rift (Fig. 7). Taking such ages as proxies for end of motion on the STDS (Grey dashed thick line 1, Fig. 7) lead to hypothesize that the Yadong rift would correspond to a major timing discontinuity, with an STDS lasting ~3 Ma longer east of the rift (Wu et al., 1998). In Buthan, Kellett et al. (Kellett et al., 2009) have proposed that the internal part of the STDS, now outcropping in South Tibet (G and W, Fig. 1a and Fig. 7, line 1b), stayed active after 11Ma, while the external part of the STDS now outcropping below the Tethyan and Chekha klippen (SK, U and L, Fig. 1a and Fig. 7 line 1a) became inactive prior to that age. However, this hypothesis only rests on U/Pb emplacement ages of deformed leucocratic melts that only define a maximum, not a true, age for the end of deformation. In many locations STDS deformations appear to progressively localize in the upper part of the shear zone and to last several Ma after the time of magmatic rocks emplacement and the end of ductile shear in the deepest parts of the shear zone. It is thus not judicious to only consider this kind of constraints.

Motion on the STDS is responsible for rapid cooling of footwall rocks, and rapid cooling ages provide a maximum age for the end of motion on the STDS that is probably closer to the real age, slowdown in cooling / exhumation rates reflecting the end of rapid motion. Taking such data in consideration suppress the need for a major step in age across the Yadong rift, whilst a general tendency of younging towards the East is possible with a major step in age of ~5 to ~3 Ma at the level of the Gurla Mandata (GM) (continuous black line 2, Fig. 7).

In few places it is possible to propose minimum ages for the end of motion on the STDS by dating crosscutting structures (S, A/D, M, G, Figs 1 &

7). Such constraints are fundamental to precisely resolve the timing of the end of deformation. However such data are still rare and often disputable. A critical example is that of the Manaslu area, where the structural cause inferred for the cooling dramatically changes the interpretation. If the cooling is related to the buckling of the STDS, as proposed by Godin (Godin et al., 2006a), the STDS has to have ended any motion by ~16 Ma which would suggest a much more complicated history (dashed black line 3 on Fig. 7). However, between the Annapurnas and Dinggye, the STDS is a continuous structure with no lateral ramps, a fact barely compatible with large variations in rate and /or duration. On the other hand, if the fast cooling is simply related to exhumation in the footwall of the Phu detachment, then a simpler history holds. One could also argue that the white micas dated at ~12 Ma (Godin et al., 2001) and ~14 Ma (Coleman and Hodges, 1995) in the Dhaulagiri area are related to late motion on STDS rather than to the Takhola normal fault, in which case the STDS could have stopped almost synchronously everywhere east of 81°E, between 12 and 11 Ma (continuous black line 2, Fig. 7), whilst a much more complicated history cannot completely be excluded (dark dashed line Fig. 7).

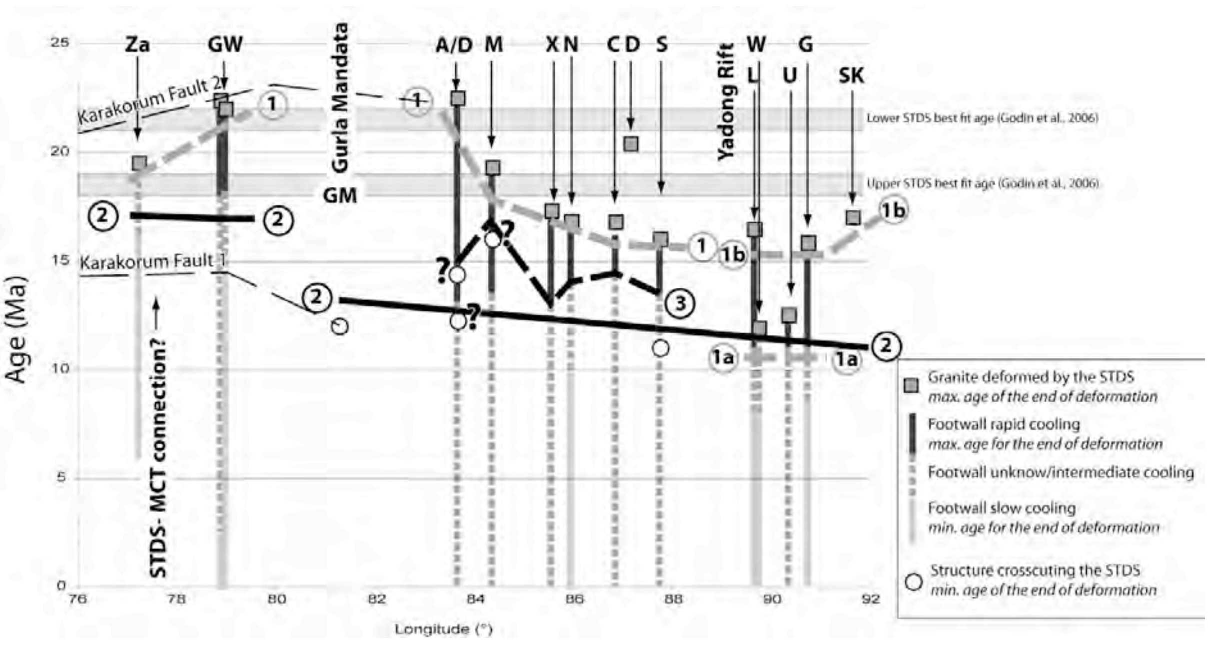

Figure 7: Timing constraints for the cessation of motion along the STDS.
Plot of timing constraints as a function of the longitude. Squares indicate U/Pb emplacement ages of magmatic rocks affected by the STDsz that yield a maximum age for the cessation of shear. Vertical bars represent local cooling histories of footwall rock of the STDS: black, rapid cooling; grey slow cooling, dashed unconstrained cooling. Rapid cooling can be interpreted to occur during STDS motion and thus yield a maximum age. Slow cooling can be interpreted as reflecting the end of exhumation and thus yield a minimum age. Open circles correspond to timing of events that occurred after the end of motion along the STDS, providing minimum ages. The best fit ages of the lower and upper STD proposed from a earliest compilation (Godin et al., 2006b) are reported as well as various hypothesis for the end of motion on the STDS. Line 1 could be proposed considering only the deformed granite ages. Lines 2 and 3 are two extreme ways to take into account most of the data. See text and Table 3 for details and references, and Fig.1a for location.

No major step in age is required in the Rothang La area, between the Zanskar shear zone and the Garwhal Himalayas STDS (~79°E, Fig. 1a) where it has been proposed that the STD merges with the MCT (Webb et al., 2007; Yin, 2006). But a ~5 to 3Ma step is apparent at the level of the Gurla Mandhata (GM, Fig. 7). The fact that this step is located, where the right-lateral Karakorum fault shows a major bend either connecting southward with the GM (e.g., Murphy et al., 2000) or continuing eastward along the Yarlung – Tzangpo suture (e.g., Lacassin et al., 2004) suggests that this fault could play a major role in the STDS history. Indeed some consider that the KF initiated prior to 22 Ma ago (Karakorum Fault 2 on Fig. 7) (Valli et al., 2008), in which case the STDS and the Karakorum fault would have been coeval for at least 4 Ma, and the interaction between the two faults could explain an earlier stop of the STDS west of the GM. However many consider that the Karakorum fault (KF) initiated less than 15.7 Ma ago (Murphy et al., 2000; Phillips et al., 2004) (Line Karakorum 1, Fig. 7), and would thus postdate end of motion on the Zanskar part of the STDS.

5.4 Why did the STDS stops at ~12 Ma ?

Combining our results with a compilation of published data leads us to infer that the STDS most likely stopped first in the west, at ~17 Ma in Zanskar but only from ~13 Ma to ~11Ma east of the GM. If true this suggests a plate-scale mechanism and interaction with the Karakorum fault to control the activity of the STDS. It is important to note that the 15-10 Ma interval corresponds to two major tectonics changes within the Himalayan belt: 1) end of major thrusting phase on the lower Main Central Thrust (MCTl) (Catlos et al., 2002a; Catlos et al., 2001; Catlos et al., 2002b; Daniel et al., 2003; DeCelles et al., 2001; Harrison et al., 1997; Kohn et al., 2004) and activation of the Main Boundary Thrust (MBT) at ~11 Ma (Meigs et al., 1995); and 2) onset of a first phase of E-W extension in southern Tibet (Arnaud et al., 2008; Dewane et al., 2006; Garzione et al., 2003; Hager et al., 2006; Kali et al., in press). This period also coincides with major changes in the India-Eurasia convergence: a change from ~N29° to ~N14° at 10-12 Ma together with a slight increase in rate from ~46 to N 50 mm/yr according to Lee and Lawyer (Lee and Lawver, 1995); or a ≥ 40% rate decrease together with a direction change between 20 and ~10 Ma for Molnar and Stock (Molnar and Stock, 2009) (Fig. 8).

The timing coincidence suggests that the changes in rate and direction of convergence is linked with the change in locus, direction and rate of thrusting in the orogenic belt, and with the switch from NNE-SSW extension (STDS) to ~E-W extension at the top of the belt. Such synchroneous change of the stress directions along ~1000km of the Himalayan belt more probably results from a sudden change in boundary conditions, not in body forces nor thermal evolution that both occur on longer time scales. It is thus more in accord with thrust wedges or thrust system models rather than mid-crustal channel flow driven by focussed erosion and high elevation of the Tibetan plateau.

In any case, while it appears fundamental to gather more data in order to more tightly constrain the timing of STDS deformations, geodynamic models have to better take into account that timing.

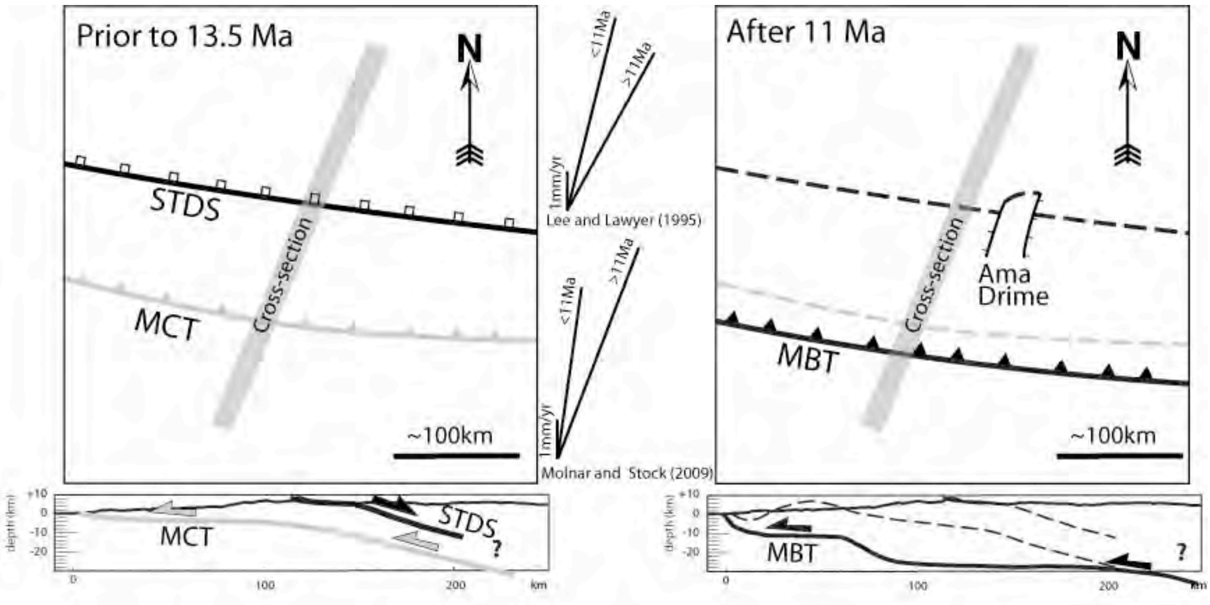

Figure 8: ~12Ma tectonic changes in central Himalaya.
Schematic maps (top) and cross-sections (bottom) prior (left) and after (right) major tectonic reorganization at ~12Ma. Structures that become inactive are dashed. Lines between the map depict the direction and amount of India -Eurasia convergence calculated from oceanic kinematics according to Lee and Lawyer (1995) (top) and Molnar and Stock (2009) (bottom).

6. Conclusion :

Combining structural, petrographical and geochronological data we demonstrated that the STDS ended its motion between 13.6 and 11 Ma ago near Dinggye, East of the Ama Drime range. Combining these data, and published ones all along the Himalayan belt, we speculate that the STDS stopped first in the west, at ~17 Ma in Zanskar but only from ~12 to ~11Ma east of the Gurla Mandata. Such timing coincides with the transition of the main thrust motion from the MCTl to the MBT, to the switch from NNE-SSW to E-W extension in southern Tibet, and to a change in the direction of the India / Eurasia convergence. This synchronism is probably better explain in the frame of a thrust wedge or thrust system model than a lower channel flow model.

Acknowledgments

We thank E. Deloule and the ion probe team of the CRPG, CNRS UPR 2300, Nancy, France for their help in dating the zircons, Claude Merlet and the electronic microprobe team of Géosciences Montpellier, Université de Montpellier 2, France, and Paul Capiez for the whole rock X-fluorence analysis at UMR 5570, Lyon, France. The field trip was financed by INSU DyETI grant to R. Lacassin and P.H.L. Reviews by An Yin and especially L. Ratschbacher helped to improve the manuscript.

Bibliography.

Armijo, R., Tapponnier, P., Mercier, J.L., Han, T.L., 1986. Quaternary Extension in Southern Tibet - Field Observations and Tectonic Implications. J. Geophys. Res. 91, 13803-13872.

Arnaud, N., Aitchison, J.C., Leloup, P.H., Valli, F., Wilde, S., 2008. Constraints on the initiation of normal faulting across the Yarlung Tsangpo suture zone, from the Lopu Gangri range, southern Tibet. Geophys. Res. Abst. 10, EGU2008-A-00000.

Beaumont, C., Jamieson, R.A., Nguyen, M.H., Lee, B., 2001. Himalayan tectonics explained by extrusion of a low-viscosity crustal channel coupled to focused surface denudation. Nature. 414, 738-742.

Bollinger, L., Avouac, J.P., Beyssac, O., Catlos, E.J., Harrison, T.M., Grove, M., Goffe, B., Sapkota, S., 2004. Thermal structure and exhumation history of the Lesser Himalaya in central Nepal. Tectonics. 23, TC5015, doi:5010.1029/2003TC001564.

Bordet, P., 1961. Recherches géologiques dans l'Himalaya du Népal, région du Makalu, CNRS, Paris.

Borghi, A., Castelli, D., Lombardo, B., Visona, D., 2003. Thermal and baric evolution of garnet granulites from the Kharta region of S Tibet, E Himalaya. Eur. J. Mineral. 15, 401-418.

Brunel, M., 1983. Etude pétro-structurale des chevauchements ductiles en Himalaya (Népal oriental et Himalaya du Nord–Ouest), University of Paris VII.

Burchfiel, B.C., Royden, L.H., 1985. North-South Extension within the Convergent Himalayan Region. Geology. 13, 679-682.

Burchfiel, B.C., Zhilang, C., Hodges, K.V., Yuping, L., Royden, L.H., Changrong, D., Jiene, X., 1992. The South Tibetan detachment System, Himalayan Orogen: Extension Contemporaneous with and Parallel to Shortening in a Collisional Mountain Belt., Geological Society of America

Burg, J.P., 1983. Carte Géologique du Sud tibet, in: M.o. Geology/CNRS, (Ed), Ministry of Geology/CNRS, Beijing/Paris.

Burg, J.P., Brunel, M., Gapais, D., Chen, G.M., Liu, G.H., 1984. Deformation of Leucogranites of the Crystalline Main Central Sheet in Southern Tibet (China). J. Struct. Geol. 6, 535-542.

Carosi, R., Lombardo, B., Molli, G., Musumeci, G., Pertusati, P.C., 1998. The south Tibetan detachment system in the Rongbuk valley, Everest region. Deformation features and geological implications. J. Asian Earth Sci. 16, 299-311.

Catlos, E.J., Gilley, L.D., Harrison, T.M., 2002a. Interpretation of monazite ages obtained via in situ analysis. Chem. Geol. 188, 193-215.

Catlos, E.J., Harrison, T.M., Kohn, M.J., Grove, M., Ryerson, F.J., Manning, C.E., Upreti, B.N., 2001. Geochronologic and thermobarometric constraints on the evolution of the Main Central Thrust, central Nepal Himalaya. J. Geophys. Res. 106, 16177-16204.

Catlos, E.J., Harrison, T.M., Manning, C.E., Grove, M., Rai, S.M., Hubbard, M.S., Upreti, B.N., 2002b. Records of the evolution of the Himalayan orogen from in situ Th-Pb ion microprobe dating of monazite: Eastern Nepal and western Garhwal. J. Asian Earth Sci. 20, 459-479.

Coleman, M., Hodges, K., 1995. Evidence for Tibetan Plateau Uplift before 14-Myr Ago from a New Minimum Age for East-West Extension. Nature. 374, 49-52.

Coleman, M.E., Hodges, K.V., 1998. Contrasting Oligocene and Miocene thermal histories from the hanging wall and footwall of the South Tibetan detachment in the central Himalaya from Ar-40/Ar-39 thermochronology, Marsyandi Valley, central Nepal. Tectonics. 17, 726-740.

Cottle, J.M., Jessup, M.J., Newell, D.L., Horstwood, M.S.A., Noble, S.R., Parrish, R.R., Waters, D.J., Searle, M.P., 2009. Geochronology of granulitized eclogite from the Ama Drime Massif: Implications for the tectonic evolution of the South Tibetan Himalaya. Tectonics. 28, DOI: 10.1029/2008TC002256.
Cottle, J.M., Jessup, M.J., Newell, D.L., Searle, M.P., Law, R.D., Horstwood, M.S.A., 2007. Structural insights into the early stages of exhumation along an orogen-scale detachment: The South Tibetan Detachment system, Dzakaa Chu section, eastern Himalaya. J. Struct. Geol. 29, 1781-1797.
Daniel, C.G., Hollister, L.S., Parrish, R.R., Grujic, D., 2003. Exhumation of the Main Central Thrust from lower crustal depths, Eastern Bhutan Himalaya. J. Metamorph. Geol. 21, 317-334.
Dasgupta, S., Ganguly, J., Neogi, S., 2004. Inverted metamorphic sequence in the Sikkim Himalayas: crystallization history, P-T gradient and implications. J. Metamorph. Geol. 22, 395-412.
DeCelles, P.G., Gehrels, G.E., Najman, Y., Martin, A.J., Carter, A., Garzanti, E., 2004. Detrital geochronology and geochemistry of Cretaceous-Early Miocene strata of Nepal: implications for timing and diachroneity of initial Himalayan orogenesis. Earth Planet. Sci. Lett. 227, 313-330.
DeCelles, P.G., Robinson, D.M., Quade, J., Ojha, T.P., Garzione, C.N., Copeland, P., Upreti, B.N., 2001. Stratigraphy, structure, and tectonic evolution of the Himalayan fold-thrust belt in western Nepal. Tectonics. 20, 487-509.
Dewane, T.J., Stockli, D.F., Hager, C., Taylor, M., Ding, L., Lee, J., Wallis, S., 2006. Timing of Cenozoic E-W Extension in the Tangra Yum Co-Kung Co Rift, south-central Tibet. American Geophysical Union fall Metting, abstract with program.
Dezes, P.J., Vannay, J.C., Steck, A., Bussy, F., Cosca, M., 1999. Synorogenic extension: Quantitative constraints on the age and displacement of the Zanskar shear zone (northwest Himalaya). Geol. Soc. Am. Bull. 111, 364-374.
Edwards, M.A., Kidd, W.S.F., Li, J.X., Yu, Y.J., Clark, M., 1996. Multi-stage development of the southern Tibet detachment system near Khula Kangri. New data from Gonto La. Tectonophysics. 260, 1-19.
England, P., Molnar, P., 1993. Cause and effect among thrust and normal faulting, anatectic melting and exhumation in the Himalaya, in: P.J. Treloar, M.P. Searle, (Eds), Himalayan Tectonics, Geological Society of London Special Publication,Geological Society of London, London, pp. 401-4011.
Ferry, J.M., Spear, F.S., 1978. Experimental Calibration of Partitioning of Fe and Mg between Biotite and Garnet. Contrib. Mineral. Petrol. 66, 113-117.
Garzione, C.N., DeCelles, P.G., Hodkinson, D.G., Ojha, T.P., Upreti, B.N., 2003. East-west extension and Miocene environmental change in the southern Tibetan plateau: Thakkhola graben, central Nepal. Geol. Soc. Am. Bull. 115, 3-20.
Godin, L., Gleeson, T.P., Searle, M.P., Ullrich, T.D., Parrish, R.R., 2006a. Locking of southward extrusion in favour of rapid crustal-scale buckling of the Greater Himalayan sequence, Nar valley, central Nepal, in: R.D. Law, M.P. Searle, L. Godin, (Eds), Channel Flow, Ductile Extrusion and Exhumation in Continental Collision Zones 268,Geological Society of London Special Publication, London, pp. 269-292.
Godin, L., Grujic, D., Law, R.D., Searle, M.P., 2006b. Channel flow, ductile extrusion and exhumation in continental collision zones: an introduction, in: R.D. Law, M.P. Searle, L. Godin, (Eds), Channel Flow, Ductile Extrusion and Exhumation in Continental Collision Zones 268,Geological Society of London Special Publication, London, pp. 1-23.

Godin, L., Parrish, R.R., Brown, R.L., Hodges, K.V., 2001. Crustal thickening leading to exhumation of the Himalayan Metamorphic core of central Nepal: Insight from U-Pb Geochronology and Ar-40/Ar-39 Thermochronology. Tectonics. 20, 729-747.
Goscombe, B., Gray, D., Hand, M., 2006. Crustal architecture of the Himalayan metamorphic front in eastern Nepal. Gondwana Res. 10, 232-255.
Goscombe, B., Hand, M., 2000. Contrasting P-T paths in the Eastern Himalaya, Nepal: Inverted isograds in a paired metamorphic mountain belt. J. Petrol. 41, 1673-1719.
Grasemann, B., Fritz, H., Vannay, J.C., 1999. Quantitative kinematic flow analysis from the Main Central Thrust Zone (NW-Himalaya, India): implications for a decelerating strain path and the extrusion of orogenic wedges. J. Struct. Geol. 21, 837-853.
Groppo, C., Lombardo, B., Rolfo, F., Pertusati, P., 2007. Clockwise exhumation path of granulitized eclogites from the Ama Drime range (Eastern Himalayas). J. Metamorph. Geol. 25, 51-75.
Grujic, D., Casey, M., Davidson, C., Hollister, L.S., Kundig, R., Pavlis, T., Schmid, S., 1996. Ductile extrusion of the Higher Himalayan Crystalline in Bhutan: Evidence from quartz microfabrics. Tectonophysics. 260, 21-43.
Grujic, D., Hollister, L.S., Parrish, R.R., 2002. Himalayan metamorphic sequence as an orogenic channel: insight from Bhutan. Earth Planet. Sci. Lett. 198, 177-191.
Hager, C., Stockli, D., Dewane, T., Ding, L., 2006. Episodic Mio-Pliocene rifting in south-central Tibet. Thermochronometric constraints from the Xainza rift. American Geophysical Union fall Metting, abstract with program.
Hames, W.E., Bowring, S.A., 1994. An empirical evaluation of the argon diffusion geometry in muscovite. Earth Planet. Sci. Lett. 124, 161-169.
Harris, N.B.W., Caddick, M., Kosler, J., Goswami, S., Vance, D., Tindle, A.G., 2004. The pressure-temperature-time path of migmatites from the Sikkim Himalaya. J. Metamorph. Geol. 22, 249-264.
Harrison, T.M., Célérier, J., Aikman, A.B., Hermann, J., Heitzler, M.T., 2009. Diffusion of 40Ar in muscovite. Geochim. Cosmochim. Acta. 73, 1039-1051.
Harrison, T.M., Duncan, I., Mc Dougall, I., 1985. Diffusion of 40Zr in biotite: temperature, pressure and compositional effect. Geochim. Cosmochim. Acta. 49, 2461-2468.
Harrison, T.M., Ryerson, F.J., LeFort, P., Yin, A., Lovera, O.M., Catlos, E.J., 1997. A Late Miocene-Pliocene origin for the Central Himalayan inverted metamorphism. Earth Planet. Sci. Lett. 146, E1-E7.
Hodges, K.V., Hames, W.E., Olszewski, W., Burchfiel, B.C., Royden, L.H., Chen, Z., 1994. Thermobarometric and Ar-40 Ar-39 Geochronological Constraints on Eohimalayan Metamorphism in the Dinggye Area, Southern Tibet. Contrib. Mineral. Petrol. 117, 151-163.
Hodges, K.V., Parrish, R.R., Searle, M.P., 1996. Tectonic evolution of the central Annapurna Range, Nepalese Himalayas. Tectonics. 15, 1264-1291.
Holdaway, M.J., 2000. Application of new experimental and garnet Margules data to the garnet-biotite geothermometer. Am. Mineral. 85, 881-892.
Holland, T., Baker, J., Powell, R., 1998. Mixing properties and activity-composition relationships of chlorites in the system MgO-FeO-Al2O3-SiO2-H2O. Eur. J. Mineral. 10, 395-406.
Holland, T.J.B., Powell, R., 1998. An internally consistent thermodynamic data set for phases of petrological interest. J. Metamorph. Geol. 16, 309-343.
Hurtado, J.M., Hodges, K.V., Whipple, K.X., 2001. Neotectonics of the Thakkhola graben and implications for recent activity on the South Tibetan fault system in the central Nepal Himalaya. Geol. Soc. Am. Bull. 113, 222-240.

Jessup, M.J., Cottle, J.M., Searle, M.P., Law, R.D., Newell, D.L., Tracy, R.J., Waters, D.J., 2008a. P-T-t-D paths of Everest Series schist, Nepal. J. Metamorph. Geol. 26, 717-739.

Jessup, M.J., Newell, D.L., Cottle, J.M., Berger, A.L., Spotila, J.A., 2008b. Orogen-parallel extension and exhumation enhanced by denudation in the trans-Himalayan Arun River gorge, Ama Drime Massif, Tibet-Nepal. Geology. 36, 587-590.

Kali, E., Leloup, P.H., Arnaud, N., Mahéo, G., Liu, D., Boutonnet, E., VanderWoerd, J., Xiaohan, L., Liu-Zeng, J., Haibing, L., in press. Exhumation history of the deepest central Himalayan rocks (Ama Drime range): key P-T-D-t constraints on orogenic models. Tectonics.

Kellett, D.A., Grujic, D., Erdmann, S., 2009. Miocene structural reorganization of the South Tibetan detachment, eastern Himalaya: Implications for continental collision. Lithosphere. 1, 259-281.

Kohn, M.J., Wieland, M.S., Parkinson, C.D., Upreti, B.N., 2004. Miocene faulting at plate tectonic velocity in the Himalaya of central Nepal. Earth Planet. Sci. Lett. 228, 299-310.

Lacassin, R., Valli, F., Arnaud, N., Leloup, P.H., Paquette, J.L., Haibing, L., Tapponnier, P., Chevalier, M.L., Guillot, S., Maheo, G., Xu, Z.Q., 2004. Large-scale geometry, offset and kinematic evolution of the Karakorum fault, Tibet. Earth Planet. Sci. Lett. 219, 255-269.

Law, R.D., Searle, M.P., Simpson, R.L., 2004. Strain, deformation temperatures and vorticity of flow at the top of the Greater Himalayan Slab, Everest Massif, Tibet. J. Geol. Soc. 161, 305-320.

Lee, T.Y., Lawver, L.A., 1995. Cenozoic plate reconstruction of Southeast Asia. Tectonophysics. 251, 85-138.

Lombardo, B., Rolfo, F., 2000. Two contrasting eclogite types in the Himalayas: implications for the Himalayan orogeny. J. Geodyn. 30, 37-60.

Ludwig, K.R., 2003. Isoplot 3.00 a geochronological toolkit for Microsoft Excel, . Berkley Geoch. Cent. Spec. Pub. 4,

Meier, K., Hiltner, E., 1993. Deformation and metamorphism within the Main Central Thrust zone, Arun tectonic Window, eastern Nepal, in: P.J. Treloar, M.P. Searle, (Eds), Himalayan Tectonics, Geological Society of London Special Publication 74,Geological Society of London, London, pp. 511-523.

Meigs, A.J., Burbank, D.W., Beck, R.A., 1995. Middle-Late Miocene (Greater-Than-10 Ma) Formation of the Main Boundary Thrust in the Western Himalaya. Geology. 23, 423-426.

Molnar, P., Stock, J., 2009. Slowing of India's convergence with Eurasia since 20 Ma and its implications for Tibetan mantle dynamics. Tectonics. 28, 10.1029/2008TC002271.

Murphy, M.A., Yin, A., Kapp, P., Harrison, T.M., Lin, D., Guo, J.H., 2000. Southward propagation of the Karakoram fault system, southwest Tibet: Timing and magnitude of slip. Geology. 28, 451-454.

Phillips, R.J., Parrish, R.R., Searle, M.P., 2004. Age constraints on ductile deformation and long-term slip rates along the Karakoram fault zone, Ladakh. Earth Planet. Sci. Lett. 226, 305-319.

Price, R.A., 1986. The southeastern Canadian Cordillera: Thrust faulting, tectonic wedging, and delamination of the lithosphere. J. Struct. Geol. 8, 239–254.

Searle, M.P., 1999. Extensional and compressional faults in the Everest-Lhotse massif, Khumbu Himalaya, Nepal. J. Geol. Soc. 156, 227-240.

Searle, M.P., Godin, L., 2003. The South Tibetan Detachment and the Manaslu Leucogranite: A structural reinterpretation and restoration of the Annapurna-Manaslu Himalaya, Nepal. J. Geol. 111, 505-523.
Searle, M.P., Parrish, R.R., Hodges, K.V., Hurford, A., Ayres, M.W., Whitehouse, M.J., 1997. Shisha Pangma leucogranite, south Tibetan Himalaya: Field relations, geochemistry, age, origin, and emplacement. J. Geol. 105, 295-317.
Valli, F., Leloup, P.H., Paquette, J.L., Arnaud, N., Li, H.B., Tapponnier, P., Lacassin, R., Guillot, S., Liu, D.Y., Deloule, E., Xu, Z.Q., Maheo, G., 2008. New U-Th/Pb constraints on timing of shearing and long-term slip-rate on the Karakorum fault. Tectonics. 27, TC5007, doi:5010.1029/2007TC002184.
Vannay, J.C., Grasemann, B., Rahn, M., Frank, W., Carter, A., Baudraz, V., Cosca, M., 2004. Miocene to Holocene exhumation of metamorphic crustal wedges in the NW Himalaya: Evidence for tectonic extrusion coupled to fluvial erosion. Tectonics. 23, DOI: 10.1029/2002TC001429
Vannay, J.C., Hodges, K.V., 1996. Tectonometamorphic evolution of the Himalayan metamorphic core between the Annapurna and Dhaulagiri, central Nepal. J. Metamorph. Geol. 14, 635-656.
Webb, A.A.G., Yin, A., Harrison, T.M., Celerier, J., Burgess, W.P., 2007. The leading edge of the Greater Himalayan Crystalline complex revealed in the NW Indian Himalaya: Implications for the evolution of the Himalayan orogen. Geology. 35, 955-958.
Wu, C.D., Nelson, K.D., Wortman, G., Samson, S.D., Yue, Y.J., Li, J.X., Kidd, W.S.F., Edwards, M.A., 1998. Yadong cross structure and South Tibetan Detachment in the east central Himalaya (89 degrees-90 degrees E). Tectonics. 17, 28-45.
Yin, A., 2006. Cenozoic tectonic evolution of the Himalayan orogen as constrained by along-strike variation of structural geometry, exhumation history, and foreland sedimentation. Earth Sci. Rev. 76, 1-131.
Zhang, J.J., Guo, L., 2007. Structure and geochronology of the southern Xainza-Dinggye rift and its relationship to the south Tibetan detachment system. J. Asian Earth Sci. 29, 722-736.

Appendix I: Petrography methodology

Whole rock composition of sample T5D19 was obtained from X-fluorescence at the Earth sciences laboratory in Lyon, France (CNRS UMR 5570, University Lyon1 and ENS of Lyon). In weight %, SiO_2, 65.42 ; TiO_2, 0.8 ; Al_2O_3, 13.33 ; Fe_2O_3, 12.45 ; MnO, 0.14 ; MgO, 2.05 ; CaO, 0.4 ; Na_2O, 0.72 ; K_2O, 2.78 ; P_2O_5, 0.18 ; LOI, 0.71 ; H_2O-, 0.1 ; Total, 99.13.

Minerals were analysed with the Cameca SX100 microprobe at the department of Geosciences of Montpellier, France (CNRS UMR 5243). Analyses are reported in Table DR3.

The studied metapelites was described in the NCKFMAS system (Spear, 1993). Perple_X'07 has been used for the calculation of pseudosections using the 2004 revised version of the internally consistent thermodynamic dataset of Holland & Powell (Holland et al., 1998). The phases considered in the calculation were: Kyanite, Sillimanite, Andalusite, K-feldspar, Plagioclase, Garnet (Alm, Pyr, Spes, Gros), Ti-Biotite, Phengite, Chlorine, Cloritoid, Cordierite, Amphibole, staurolite and Quartz. Phases and end-members used in the solid-solution models involved in these pseudosections are from Newton et al. (Newton et al., 1980) for plagioclase, White et al. (White et al., 2007) for Ti-biotite, White et al. (White et al., 2000) for garnet and cloritoid, Holland et al. (Holland and Powell, 1998) for chlorine, Holland & Powell (Holland et al., 1998) for phengite and staurolite, Dale et al. (Dale et al., 2000) for amphibole and an ideal solution model for cordierite. Because of the high SiO_2 content, pseudosections were computed considering SiO_2 saturation. The calculation was performed with H_2O saturation.

Appendix II: geochronology

II-1 U/Pb in situ SIMS dating

Zircon and monazite grains were separated using heavy liquids, a Frantz magnetic separator and finally by hand picking under a binocular microscope avoiding the most obvious metamicts or dirty grains. The selected grains were mounted together with standard in epoxy resin. The mounts were then abraded and polished to expose at the surface the middle part of the crystals. G91500 zircon standard (Wiedenbeck et al., 1995) and WB.T.329 monazite standards (Williams, 1996) were used. Zircon and monazite grains were imaged using optical and cathodoluminescence (CL) microscopy. Monazites were analysed with the sensitive high resolution ion microprobes (SHRIMP II) at the Institute of Geology of Beijing, China, while zircons were measured using the Cameca IMS 1270 at CRPG in Nancy, France. Calibration parameters, data acquisition and age correction are described in Compston et al. (Compston et al., 1984) for the SHRIMP II, and in Deloule et al. (Deloule et al., 2001) for the Cameca IMS 1270. The error on the calibration curve is taken into account for the age uncertainty calculation. The spot size was between 30 and 60 μm.

Ion probe U-Th-Pb dating of young minerals is an analytical challenge because of the very small amounts of radiogenic daughter isotopes (^{206}Pb, ^{207}Pb, ^{208}Pb). In case of recent minerals, it is now usual for most geochronologists to consider the ^{238}U/^{206}Pb ages as the most reliable for zircons (e.g., Stern and Amelin, 2003)), and the ^{232}Th/^{208}Pb ages for monazites (e.g., Catlos et al., 2004)). The isotopic systems of zircons and, to a lesser extent, monazites keep the memory of several distinct magmatic, metamorphic and hydrothermal events. This provides the opportunity to reconstruct complex geological histories but requires cautious interpretation of the analytical results to individualize the different populations.

Within a given population of ion probe data, it is important to distinguish meaningful ages from outliers, which can always occur in spite of careful selection of rocks and minerals, and of rigorous analytical conditions. Age disparity around a mean value may results either from (1) an overlap of the probe beam on zones of distinct ages, (2) large SIMS analytical errors related to low radiogenic Pb content in young zircon overgrowths (Stern, 1997), (3) the occurrence of common Pb, (4) ^{230}Th radioactive disequilibrium in monazites (Scharer et al., 1986), (5) a partial lead loss due to (a) subsequent high temperature event(s), (6) a combination of these points. Consequently, we consider that the best age estimate of a given population of ion probe data is its mathematical mean with a two standard deviation uncertainty, which will lower the influence of outlier(s).

The Tertiary SIMS data are plotted in a Tera-Wasserburg diagram (Tera and Wasserburg, 1972) (1σ error errors for readability) while others data are plotted in concordia diagrams (1σ ellipse errors or larger symbols when ellipses are too small). Errors mentioned in the text are at the 1σ level, the weighted averages, and the associate 95% confidence errors, were calculated with Isoplot 3.23 of Ludwig (2003).

II-2 ^{40}Ar/^{39}Ar dating

Minerals were separated using heavy liquids, a Frantz magnetic separator and finally by hand picking under a binocular microscope. The samples were irradiated in two batches during april and december 2007 at the McMaster Nuclear Reactor in the 5C position for 26 h with an approximate 10^{18} neutrons $cm^{-2}s^{-1}$ flux. Irradiation interference on K, Ca and Cl were corrected by irradiating and analyzing KCl and CaF_2 pure salts. J factors were estimated by the use of duplicates of the Fish Canyon sanidine standard with an age of 28.02 Ma (Renne et al., 1998).

The samples were analyzed in Montpellier using the same apparatus and the same protocol, as described in Arnaud et al. (2003). Samples were loaded in aluminum packets into a double vacuum Staudacher type furnace and step heated; temperature is calibrated by means of a thermocouple. The gas was purified using cold traps with liquid air and Al-Zr getters. Once cleaned, the gas was introduced into a VG3600 mass spectrometer and allowed to equilibrate for 2 min prior to analysis was done statically. Signals were measured by the mean of a Faraday cup with a 10^{11} ohm resistor for ^{40}Ar and ^{39}Ar while ^{39}Ar, ^{38}Ar, ^{37}Ar and ^{36}Ar were analyzed with a photomultiplier after interaction on a Daly plate. Gain between both collectors was estimated by duplicate analysis of ^{39}Ar on both collectors during each analysis, and also by statistical analysis over a period of several years. This gain is 50 and is known at better than 1.5%. This error is included in the age calculation, along with analytical errors on each signal and errors on the blank values. Age plateau given are weighted mean plateaus; the error takes the error on the J factor into account. With the historical decrease of analytical errors, strict plateau criteria (Berger and York, 1981; Dalrymple and Lanphere, 1974) are less frequently met. Thus, pseudoplateaus are used when a significant number of steps overlap globally at 2σ even if contiguous steps do not. Isochron ages are obtained on an inverse isochron diagram of $^{36}Ar/^{40}Ar$ versus $^{39}Ar/^{40}Ar$ (Roddick, 1978; Roddick et al., 1980), which often allows homogeneous excess components to be identified. Errors on age and intercept age include individual errors on each point and linear regression by York's method (York, 1969). The goodness of fit relative to individual errors is measured by Mean Square Weighted Deviation (MSWD).

Classical furnace step heating was conducted and plateau and isochron ages were calculated. If the inverse isochron age is close to the plateau age and $^{40}Ar/^{36}Ar$ is not significantly different from present day $^{40}Ar/^{36}Ar$ atmospheric ratio (295.5), we consider that the plateau age is reliable. When this is not the case, we suspect a non-atmospheric initial $^{40}Ar/^{36}Ar$ ratio and we thus prefer to rely on the inverse isochron age if this one is well determined. All errors are quoted at 2 sigmas.

Appendix III: published timing constraints on STDS cessation of shear.

Description from east to West. See Fig. 1a for location. Data summarized in Table DR7 and on Fig. 7.

In the Gonto La valley (G on Fig. 1a), the ~300m thick Gonto La detachment affects the Khula Kangri leucogranite (Edwards et al., 1996). A sample from the lowermost part of the shear zone yields a $^{208}Pb/^{232}Th$ monazite age of 12.5±0.4 Ma implying that the STDS was active after that age at this location (Edwards and Harrison, 1997). Biotites and muscovites from the leucogranites yield ages around 11Ma (Maluski et al., 1988) suggesting rapid cooling at that time probably related to exhumation of the STDS footwall.

Farther South, the STDS outcrops below Tethyan Sedimentary Sequence klippen of the Cheka formation in Bhutan (e.g., Grujic et al., 2002). The 22-17 Ma crystallization age of a leucogranite dyke from the Sakteng klippe (SK on Fig. 1a) provides a maximum age for deformation in the STDS (e.g., Grujic et al., 2002). In the Ura klippe (U on Fig. 1a) the ~16 Ma age of a boudinated leucogranite sill yield an upper age to the end of shearing (Kellett et al., 2009).

A cooling history built from these U/Pb result, a Muscovite Ar/Ar and apatite fission tracks ages suggest a major slowdown of cooling between 11 and 8.6 Ma (Kellett et al., 2009) that could be interpreted at the end of STD motion (Fig. 7). In that area the STDS appear to be offset by the Kahtang thrust which has been active after 14-15Ma as it deforms migmatites of that age (Daniel et al., 2003; Grujic et al., 2002). (Kellett et al., 2009) propose that the outer STD, outcropping at the base of the klippen, stopped prior to ~11Ma; while the Kathang thrust initiated and the inner STD outcropping further north, continued to be active after that date. However, in the absence of more precise dating constraints this scenario stays speculative and the inner and outer STD may have been the same structure stopping soon after 11Ma and later offset by the Kathang thrust. A situation possibly comparable to Nepal where Tethyan Sedimentary klippen outcrop in the external part of the orogen (Fig. 1a) and the MCT may have been reactivated out of sequence in the late Miocene / Pliocene (Catlos et al., 2004).

East of the Yadong graben, the Wagye La leucogranite (W, Fig. 1a) is affected by the STDS (Wagye La detachment) and yield an average $^{235}U/^{207}Pb$ age of 11.9 Ma for four reversely discordand monazites, suggesting that top to the north deformation lasted after ~12 Ma (Wu et al., 1998). Zircons from a pre to synkinematic dyke within the Cheka group, intruded by the Wagye La leucogranite, yield rim ages between 11 and 82 Ma the youngest age being interpreted as the timing of the dyke emplacement (Kellett et al., 2009). However the age population shows a very clear peak at 12 Ma and the age of the dyke is probably not significantly different from that of the leucogranite. Further south, Tethyan sediments outcrop in the Lingshi klippe (L, Fig. 1a) above the STD shear zone (Kellett et al., 2009). Zircons from four deformed leucogranite sills yield rim age ranges of 21.1-31.3, 16.5-26.6, 16.9-28.9 and 16.6-24.6 Ma respectively (Kellett et al., 2009). Taking the youngest ages as the sill emplacement age, suggest ductile deformation until at least 16.5 Ma (Kellett et al., 2009). Cooling histories built from these U/Pb results, Muscovite Ar/Ar and apatite fission tracks suggest a major slowdown of cooling between ~11 and 8 Ma (Kellett et al., 2009) that could be interpreted at the end of STD motion between this dates (Fig. 7).

West of the Yadong Grabben, the STDS appears offset of ~50 km to the south (Zherger La detachment, Z on Fig. 1a). Multigrain monazite analysis from the little deformed Gaowu granite outcropping ~25 km south of the detachment, yielded U/Pb ages ranging from 272 to 24.1 Ma, while a single grain yielded a $^{235}U/^{207}Pb$ age of 22.9±0.17 Ma interpreted as the best estimate of the granite age (Wu et al., 1998). The lack of clear relationship between this granite and the STDS prevent to use that age as a constraint on its timing.

As discussed in section 5.1, end of motion along the STDS is constrained to occur between ~ 13.6 and 11 Ma near Saer (S on Fig. 1a).

~50 km to the west, of the Saer area, in the Dzakar Chu valley (D on Fig. 1a and Fig. 7; star 3 on Fig. 2a), monazites of two undeformed dykes within the STD shear zone and crosscutting the foliation have been dated (Cottle et al., 2007). They yield ages of 20.4±0.6 Ma and 16.7±0.3 Ma suggesting that deformation linked with the STDS ended prior to ~20.4 Ma at that location (Cottle et al., 2007). At first glance such timing could appear contradictory to our results. However these samples comes from ~1000 m below the STD and it is possible that, as suggested by the authors, deformation lasted longer in the STDsz above, or below, the samples. ~17km further east in the same valley, and ~7km structurally below the STD (Fig. 2a star 2), a deformed leucogranitic dyke has an age of 12.5±0.2 Ma while a deformed one is 15.2±0.2 Ma suggesting that the deformation took place between these two dates (Cottle et al., 2009). It is however not very clear if that deformation is related to the STDS or to later folding.

Farther east at the foot of the Chomolangma, leucogranites from the vicinity of the Rongbuk village (star 4 on Fig. 2b; C on Fig. 1a and Fig.9) have been dated and the corresponding constraints for STDS deformation timing have been discussed. Hodges et al. (1998) proposed that the Rongbuk granite crosscuts the Qomolangma detachment (QD). A float block sample thought to be derived from this granite yields U-Th-Pb monazites and zircon ages between 19.5 and 22 Ma together with Paleozoic – Proterozoic inheritance, (Samples _33a & b, Copeland et al., 1990; Hodges et al., 1992; Parrish, 1990). These ages are significantly older than the 16.67±0.04 Ma mean $^{207}Pb/^{235}U$ age of the youngest fraction of monazite, zircon and xenotime obtained from a deformed sill (R113) sampled 200m below the detachment (Hodges et al., 1998). This led Hodges et al. (1998) to consider the 16.37±0.4 Ma inverse isochron $^{40}Ar/^{39}Ar$ age of Δ33b muscovites as a conservative minimum estimate for the timing of cristallization of the Rongbuk granite and thus for the end of motion along the STD. However, Murphy and Harrison (1999) produced a detailed map of the area and documented that no granite crosscut the QD. They distinguished at least two leucogranite generations: one mylonitic parallel to the footwall foliation crosscut by variably deformed dykes. All dykes yield essentially the same $^{208}Pb/^{232}Th$ ion probe monazite ages: 16.8±0.8 Ma for a crosscutting dyke, 16.4±0.6 Ma for a crosscutting but deflected dyke and 16.2±0.8 Ma for a mylonitic dyke (Murphy and Harrison, 1999). They thus proposed that the QD was active at c. 17 Ma. Deeper in the UHCS unit, monazites and zircons have been dated in gneiss, deformed leucogranites and undeformed leucogranites in the Kangshung valley ~3.5 structurally below the QD (6 Fig. 2a) (Cottle et al., 2009). The ages of deformed and undeformed leucrogranites suggest that deformation ended between 20.9±0.4 and 16.7±0.4 Ma. The picture that emerge is that of a thick shear zone where leucogranites emplaced since at least 22Ma, and where shearing become more localized with time allowing the younger generation of granites to cut across the shear zone fabrics but to be deformed themselves immediately below the QD that stayed active after 16.2±0.8 Ma. Such data do not constrain the cessation of slip on the STDS. Muscovite Ar/Ar ages in the leucogranites whether they are deformed or not are in the range 16.5 – 14.8 Ma (Carosi et al., 1998; Hodges et al., 1998) suggesting footwall rapid cooling at that time. Below the summit of the Chomolangma the STD outcrop at ~8520m asl above the metamorphosed limestones of the yellow band formation (Sakai et al., 2005). Apatite and zircon FT ages from this formation suggest very rapid cooling from 350°C to 130°C at ~14.4 Ma (Sakai et al., 2005) that can suggest that the STD was still active at that time.

~65 km East of Rongbuk, the Nyalam section (N on Fig. 1a) of the STDS has been described by Burchfiel et al. (1992). Monazites from a migmatitic granite deformed in the footwall of the STDS (sample XGS121) yield a 16.8±0.6 Ma U/Pb age (Scharer et al., 1986) suggesting that the STDS was active after that time. $^{40}Ar/^{39}Ar$ muscovite ages range from the STDsz and its footwall is 16.1-15.2, while that of biotite is 15.6 – 14.8 Ma (Wang et al., 2006). Argon K-feldspar multidomain diffusion modelling suggest rapid cooling between ~16 and ~14 Ma (Wang et al., 2006). Apatite FT ages span between 11.9±2.1 and 9.7±0.7 Ma (Wang et al., 2001) suggesting that very limited exhumation (≤ 3km) has occurred since ~10 Ma. The data are interpreted as reflecting a transition from rapid to slow cooling between 11.7 and 9.7Ma (Wang et al., 2006). Such transition could be interpreted as the timing of the end of motion along the STDS.

25 km east the Nyalam section the STDS cuts the XixaPangma leucogranite (X on Fig. 1a). While a weakly foliated granite immediately below the STDS yields 20.2±0.2 Ma U/Pb xenotime and monazite ages, the main granite body yields U/Pb zircon, uraninite and monazite ages of 17.3±0.2 Ma and a 16.7±0.2 Ma plateau $^{40}Ar/^{39}Ar$ muscovite age strongly suggesting that the STDS has been active after ~17 Ma (Searle et al., 1997). Apatite fission track ages for the main granite body sampled from 5800 to 8000 m elevation, range from 12.3±1.9 to 14.8±0.8 Ma (Searle et al., 1997). Such results could possibly indicate a rapid cooling until ~13 Ma but uncertainties are large and the age elevation plot tend to show younger ages at high altitudes which is not easy to interpret.

In the Manaslu area (M, Fig. 1a), two top to the north normal faults have been described: the ductile and brittle Phu detachment, and farther south the ductile Chame detachment (e.g., Godin et al., 2006). The rocks comprised between the two detachments are metamorphosed limestone and calc-silicate mostly belonging to the Annapurna Formation (Colchen et al., 1986; Searle and Godin, 2003). These rocks are interpreted as the metamorphosed sedimentary cover of the GHS (Colchen et al., 1986; Guillot et al., 1995; Searle and Godin, 2003) and then as stratigraphically belonging to the base of the Tethyan Unit. In this case the Chame detachment is interpreted as the main strand of the STDS (Colchen et al., 1986). However, based on its high metamorphic grade some authors include the Annapurna formation in the Greater Himalayan Sequence (Godin et al., 2006; Searle and Godin, 2003). Moreover, there is no major metamorphic contrast across the Chame detachment (Coleman and Hodges, 1998; Godin et al., 2006; Guillot et al., 1995; Searle and Godin, 2003). This lead to the conclusion that the main, and more recent, strand of the STDS is the Phu detachment that separates greenschist facies rocks (~300°C) from unmetamorphosed sediments (Searle and Godin, 2003). The Chame detachment and the Annapurna formation are affected by an antiform with an E-W axis (Godin et al., 2006). The Manaslu leucogranite is a large body intrusive within the Annapurna formation. The granite is affected by high temperature top to the North normal deformation (e.g., Guillot et al., 1993) and is mapped by some as crosscutting the Phu detachment (Colchen et al., 1986; Guillot et al., 1993), while other consider that the granite is affected and toped by the Phu detachment (Searle and Godin, 2003). Th-Pb monazite ages from the Manaslu granite indicate two major magmatic events at 22.9 ± 0.6 Ma and 19.3 ± 0.3 Ma (Harrison et al., 1999). Dykes apparently feeding the Annapurna granite crosscut the Chame detachment (Harrison et al., 1999). These particular dykes have not been dated, but similar dykes have been dated at 18-19 Ma (Coleman, 1998). Hornblende, muscovite, biotite, and K-feldspar Ar/Ar ages in the Manaslu granite and Annapurna formation span from ~23 to ~13.5 Ma (Copeland et al., 1990; Godin et al., 2006; Guillot et al., 1994; Harrison et al., 1999). Such ages have been interpreted as reflecting either the cooling following the granite intrusion (Copeland et al., 1990), unroofing linked to normal fault(s) located north of the Manaslu (Guillot et al., 1994), or the buckling of the Annapurna formation and of the Chame detachment (Godin et al., 2006). From these studies, it can be concluded that deformation on the Chame detachment ended prior to the emplacement of the Manaslu granite from 23 to 19 Ma. Timing of the end of motion on the Phu detachment is more controversial: prior to 19 Ma if it is crosscut by the Manaslu granite (Guillot et al., 1994; Harrison et al., 1999) or after that date if it affects the granite (Searle and Godin, 2003). Godin et al., (2006) propose that the Phu detachment was inactive prior to 16 Ma ago as they interpret the cooling ages as related to the buckling that affect the detachment. Coleman and Hodges (Coleman and Hodges, 1998) interpret the 14.3±0.4 Ar/Ar Age of muscovites within vertical ~N-S tension gashes as the timing of initiation of the Takhola fault system, thus postdating the end of motion on the STDS. However, such tension gashes may have formed under ~N-S compression not necessarily E-W extension, and the bulk of the cooling ages could rather suggest that exhumation linked to the Phu Chu detachment may have lasted until at least 13.5 Ma.

In the western Annapurna / Dhaulagiri area (A/D Fig. 1a) a major, ~1500m thick, top to the north normal shear zone affects amphibolite to upper greenschist facies calc-silicate and limestone (Colchen et al., 1986; Godin, 2003; Godin et al., 1999; Pêcher and LeFort, 1986). The Calc-silicate and limestone are interpreted as the paleozoic sedimentary cover of the GHS and can be consider as lateral equivalent of the metamorphosed Tethyan rocks comprised between the Chame and Phu detachment observed in the Manaslu area (Hodges et al., 1996; Searle and Godin, 2003). Thus in the west Annapurna area the two detachments recognized in the Manaslu area merge in a single shear zone. A transitional area has been described along the Modi Khola by Hodges et al. (Hodges et al., 1996) were amphibolitic Tethysian limestone outcrop between the Deorali detachment (equivalent of the Chame detachment) and the Machhapuchhare detachment (equivalent of the Phu detachment). A 22-23 Ma (Monazite U-Pb) crystallisation age for an undeformed leucogranites crosscutting the base of the 1500m thick top to the North normal deformation within the Annapurna shear zone indicate that normal motion stopped in the basal part of the detachment before that time but probably lasted longer upsection (Godin et al., 2001). Most Ar/Ar muscovite ages from the shear zone span between 15.5 and 13.1 Ma (Godin et al., 2001; Vannay and Hodges, 1996) suggesting that deformation lasted until 13.1 Ma. Two younger ages at 11.8 and 12.7 Ma have been interpreted as late hydrothermal activity associated with the N-S Thakkhola grabben (Godin et al., 2001). However such hydrothermal activity could as well be associated with late brittle motion within the Annapurna sz.

In the Gurla Mandhata area (GM Fig. 1a) the STDS is offset by the N-S striking Gurla Mandhata detachment (Murphy and Copeland, 2005). That detachment was active at least between 11.4 and 6.8 Ma according to U-Th/Pb monazite ages of synkinematic dykes (GM5 & GM6) and 12 to 7 Ma micas Ar ages of granites and mylonites (Murphy et al., 2002). Significant top to the North motion thus appears to have stopped in that area prior to ~12Ma.

In the Garhwal area (GW Fig. 1a), the ~22-23 Ma old (U-Pb mz) Shivling leucogranite is affected by STDS related deformation (Harrison et al., 1997; Searle et al., 1999) implying that the STDS is still active after ~22 Ma. Muscovite K/Ar together with apatite and zircon fission tracks ages suggest that following a phase of fast cooling around 22-18 Ma cooling slows down somewhere between 18 and 14 Ma (Searle et al., 1999; Sorkhabi et al., 1996) suggesting that the STDS may have stopped at that time. The Gango Tri granite shows a very similar cooling history with a 22.4±0.5 Ma emplacement (Harrison et al., 1997), followed by a rapid cooling until at least 18 Ma (Sorkhabi et al., 1996).

In the Zanskar area (Za, Fig. 1a) the STDS corresponds to the ~1000 m thick Zanskar shear zone separating the slightly deformed Tethyan rocks from the HCS rocks (e.g., Dezes et al., 1999). U/Pb dating of accessory minerals give ages between 22 and 19.5 Ma for partial melting and magmatism for the Gulburanjun granite in the footwall of the STDS (Dezes et al., 1999; Walker et al., 1999). Undeformed pegmatitic dykes crosscutting the Zanskar the shear zone, ~800 m below the STD, also emplaced at ~22Ma (Walker et al., 1999), implying that ductile deformation in the bottom part of the STDS ended prior to ~22 Ma. Biotite, muscovite Ar/Ar , K/Ar and Rb/Sr dating from rocks within and directly below the shear zone indicates a very fast cooling until ~19 Ma (Dezes et al., 1999; Ferrara et al., 1991; Walker et al., 1999) that can be interpreted as related to rapid motion along the STDS. The lower temperature part of the history is not constrained, but compilation of thermochronologic data in Zanskar in the GHS further south from the STDS suggests a slow cooling between 16 and 5 Ma (Sorkhabi et al., 1997).

Table DR1 : micro-structural data
Listing of foliation and lineation attitudes. Data plotted on Fig. 2b and Fig. 3.

Table DR2 : samples location and rock types.
Facies and location of samples used in this study. For map location see Fig. 2b.

Table DR3 :Mineral data
Weight oxide (%), cations p.f.u. and X_{Fe} [(Fe/Mg+Fe)] and / or mineralogic end-members %, as calculated for each electronic microprobe measurement for garnet, biotite, staurolite and plagioclase. Fe^{3+} has been calculated by stoichiometry.

Table DR4: U/Pb zircons detailed data
Data plotted on Fig. 5a to f.
Table DR4-1: sample T5D21.
Table DR4-2: sample T5D20.

Table DR5: U/Pb monazite detailed data
Data plotted on Fig. 5g to j.
206*: radiogenic Pb, comm206: common Pb. TW: Tera-Wasserburg.
Table DR5-1: sample T5D20.
Table DR5-2: sample T5D21.

Table DR6: Argon detailed data.
40Ar*: radiogenic 40Ar
Table DR6-1: biotites (samples T5D19 and T5D21).
Table DR6-2: muscovites (sample T5D20 and T5D21

Table DR7: Synthesis of available timing constraints on the cessation of motion along the STDS.
See appendix III for details. Data are plotted on Fig. 7. Mz: monazite, Mu: muscovite, Biot : biotite, Ap: apatite, Zr: zircon

general location	GPS outcrop	GPS handset UTM coordinates (zone 45R) easting	nording	altitude (m)	rock type	structure	plane strike & dip	direction Azimuth or pitch	sense
STDsz Dzakar Chu	7-74	536333	3127952	3755	micaschists and gneiss	foliation	N090 12N	/	
	7-22	527382	3134169	3883	micaschists and defomed leucogranites	foliation / lineation	N080 45N	P 45E	
	7-75	525128	3134736	3910	defomed leucogranite	foliation / lineation	N070 50N	P 10E	
					defomed leucogranite	foliation / lineation	N080 45N	P 22E	
					micaschists	foliation	N083 50N	/	
					micaschists	foliation	N075 53N	/	
	7-21	522482	3135439	3976	micaschists and defomed leucogranites	foliation / lineation	N055 10N	Az 30	top to theN
STDsz Saer	219	569208	3116088	4569	deformed leucogranite	foliation / lineation	N020 48W	Az 018	
					deformed leucogranite	foliation / lineation	N035 30W	Az 030	
					micaschist and leucogranite	brittle fault plane	N000 55E		
	218	570346	3115866	4451	micaschist	foliation / lineation	N030 45W	Az 27	
					orthogneiss	foliation / lineation	N010 43W	P 20S	top to theN
					deformed leucogranite	foliation / lineation	N010 45W	P 23S	top to theN
					deformed leucogranite	foliation / lineation	N002 65W	P 22S	
	182	572937	3118477	4284	deformed leucogranite	foliation / lineation	N036 40W	Az 044	
	222	576656	3117898	4263	Garnet micaschist	foliation / lineation	N020 08W	Az 020	top to theN
					Garnet micaschist	foliation / lineation	N000 14W	Az 015	top to theN
					Garnet micaschist	foliation / lineation	N100 12S	Az 020	top to theN
	220	580542	3116399	4399	Ordovician sandstones	S0/S1 - lineation	N110 14N	Az 030	top to theN

Table DR1

Samples	GPS outcrop	UTM coordinates (zone 45R) easting	nording	Altitude	rock type	Geochronology and petrology
T5D19b	222	576656	3117898	4263	garnet-sillimanite micaschist	**Ar/Ar** (bio); **Petrology**
T5D20	222	576656	3117898	4263	deformed leucogranite	**U/Pb** (zr IMS1270 Nancy, mz SHRIMP Bejing); **Ar/Ar** (bio, mu)
T5D21	222	576656	3117898	4263	undeformed leucogranite	**U/Pb** (zr IMS1270 Nancy, mz SHRIMP Bejing); **Ar/Ar** (mu)

Table DR2

Representative composition of garnet

Garnet T5D19b, Fig. 5c profile	A												B
Zone	II	II	II	I	I	I	I	I	I	I	I	II	II
SiO2	38.05	37.90	39.36	37.31	37.32	37.50	37.34	38.36	37.45	37.70	36.77	38.74	37.87
Al2O3	21.84	21.61	22.32	21.19	21.24	21.71	21.36	21.74	21.63	21.55	20.94	21.79	21.82
MgO	2.31	2.32	2.10	2.15	1.88	1.80	1.81	1.80	1.84	1.85	1.98	2.12	2.17
FeO	38.41	38.86	38.36	37.94	38.04	37.45	37.28	37.68	37.97	37.52	37.06	38.01	37.92
MnO	0.85	0.71	0.80	0.80	0.97	1.14	1.18	1.30	1.36	1.30	1.28	1.30	1.62
Cr2O3	0.02	0.03	0.02	-0.01	-0.02	0.02	0.00	0.04	0.02	0.00	0.02	0.02	-0.01
TiO2	0.04	0.02	0.25	0.04	0.03	0.01	0.01	0.05	0.07	0.03	0.02	0.02	0.00
NiO	0.00	0.03	0.02	0.00	0.01	0.00	-0.01	0.00	0.02	0.00	0.02	0.02	-0.03
CaO	0.88	0.98	1.24	1.91	2.02	2.09	2.09	2.07	1.86	1.79	1.97	1.55	1.05
Na2O	0.05	0.02	0.02	0.03	0.07	0.05	0.08	0.03	0.03	0.08	0.09	0.06	0.01
K2O	0.01	0.01	0.00	0.00	0.01	0.00	0.02	0.01	0.00	0.01	0.01	0.00	0.00
∑ oxydes	102.45	102.49	104.49	101.37	101.57	101.77	101.17	103.08	102.24	101.83	100.16	103.63	102.42
Site T													
Si	6.02	6.00	6.11	5.97	5.96	5.97	5.99	6.04	5.95	6.01	5.95	6.06	6.00
Al IV	-0.02	0.00	-0.11	0.03	0.04	0.03	0.01	-0.04	0.05	-0.01	0.05	-0.06	0.00
Site O													
Al VI	4.09	4.03	4.19	3.96	3.97	4.05	4.02	4.07	4.00	4.05	3.95	4.08	4.07
Cr	0.00	0.00	0.00	0.00	0.00	0.00	0.00	0.01	0.00	0.00	0.00	0.00	0.00
Ti	0.00	0.00	0.03	0.00	0.00	0.00	0.00	0.01	0.01	0.00	0.00	0.00	0.00
	4.10	4.04	4.22	3.97	3.97	4.06	4.02	4.08	4.01	4.05	3.95	4.08	4.07
Site A													
Mg	0.54	0.55	0.48	0.51	0.45	0.43	0.43	0.42	0.44	0.44	0.48	0.49	0.51
Fe	5.08	5.14	4.98	5.08	5.08	4.99	5.00	4.96	5.04	5.00	5.02	4.97	5.02
Mn	0.11	0.10	0.11	0.11	0.13	0.15	0.16	0.17	0.18	0.17	0.18	0.17	0.22
Ni	0.00	0.00	0.00	0.00	0.00	0.00	0.00	0.00	0.00	0.00	0.00	0.00	0.00
Ca	0.15	0.17	0.21	0.33	0.35	0.36	0.36	0.35	0.32	0.31	0.34	0.26	0.18
Na	0.02	0.01	0.01	0.01	0.02	0.01	0.03	0.01	0.01	0.03	0.03	0.02	0.00
K	0.00	0.00	0.00	0.00	0.00	0.00	0.00	0.00	0.00	0.00	0.00	0.00	0.00
∑	5.90	5.96	5.78	6.03	6.03	5.94	5.98	5.92	5.99	5.95	6.05	5.92	5.93
% Alm	87.98	87.81	87.80	85.82	86.49	86.43	86.33	86.55	87.03	87.03	85.96	86.84	87.94
% Gros	2.60	2.83	3.65	5.53	5.89	6.18	6.19	6.10	5.46	5.32	5.86	4.53	3.11
% Pyr	9.42	9.36	8.55	8.65	7.62	7.39	7.47	7.35	7.51	7.65	8.18	8.63	8.95

Representative composition of biotite

Inclusion within garnet (Inc) and in foliation (Fol)

Sample	T5D19b	T5D19b	T5D19b	T5D19b	T5D19b
Localisation	Inc	Inc	Inc	Fol	Fol
SiO2	34.49	34.53	33.96	35.79	36.32
Al2O3	18.92	19.11	19.41	19.90	19.46
FeO	24.09	25.01	25.92	21.96	22.90
MnO	0.06	0.06	0.10	0.06	0.06
MgO	5.84	6.15	5.07	6.42	6.14
CaO	0.10	0.06	0.00	0.26	0.20
Na2O	0.19	0.28	0.29	0.11	0.24
K2O	9.52	9.32	9.32	9.04	9.04
TiO2	2.07	1.82	1.85	1.26	1.21
Total	95.28	96.33	95.91	94.79	95.59
Si	5.47	5.43	5.40	5.59	5.65
Al tet	2.53	2.57	2.60	2.41	2.35
Al octa	1.01	0.97	1.03	1.26	1.22
Fe^{2+}	2.84	2.92	3.06	2.55	2.65
Fe^{3+}	0.03	0.03	0.03	0.03	0.03
Mg	1.38	1.44	1.20	1.50	1.42
Ti	0.25	0.21	0.22	0.15	0.14
Mn	0.01	0.01	0.01	0.01	0.01
Li	0.00	0.00	0.00	0.00	0.00
K	1.93	1.87	1.89	1.80	1.79
Na	0.06	0.08	0.09	0.03	0.07
X_{Fe}	0.68	0.67	0.72	0.63	0.65

Representative composition of staurolite

Sample	T5D19b	T5D19b	T5D19b
Al2O3	56.43	56.12	54.75
SiO2	29.11	27.55	27.76
TiO2	0.51	0.38	0.54
Na2O	-0.03	0.01	-0.02
MgO	0.93	0.92	0.87
Cr2O3	0.05	0.03	0.05
MnO	0.16	0.14	0.17
FeO	14.63	14.57	14.68
K2O	0.01	0.00	-0.01
CaO	0.01	0.00	0.00
NiO	-0.02	0.03	0.01
Total	101.83	99.75	98.84

Representative composition of plagioclase

Sample	T5D19b	T5D19b	T5D19b
SiO2	65.08	65.67	65.76
Al2O3	22.02	21.86	21.95
MgO	-0.01	0.00	-0.01
FeO	0.04	0.14	0.01
MnO	-0.01	0.00	0.01
Cr2O3	0.01	0.00	-0.01
TiO2	0.03	0.02	0.01
NiO	0.01	-0.02	0.00
CaO	2.14	2.25	1.92
Na2O	10.63	10.15	10.81
K2O	0.09	0.10	0.07
Total	100.01	100.15	100.54
Site T			
Si	2.86	2.87	2.87
Al	1.14	1.13	1.13
Site A			
Mg	0.00	0.00	0.00
Fe	0.00	0.01	0.00
Mn	0.00	0.00	0.00
Cr	0.00	0.00	0.00
Ti	0.00	0.00	0.00
Ni	0.00	0.00	0.00
Ca	0.10	0.11	0.09
Na	0.91	0.86	0.91
K	0.00	0.01	0.00
∑	1.01	0.98	1.01
% Ab	0.90	0.89	0.91
% An	0.10	0.11	0.09
% Or	0.00	0.01	0.00

Table DR3

Sample name	spot name	crystal	spot location b: border c: core	Age (Ma) 206/238	± (1σ)	Age (Ma) 207/235	± (1σ)	Age (Ma) 207/206	± (1σ)	206/238	± (%)	207/235	± (%)	207/206	± (%)	Used in concordia	Used in TW	U (ppm)	Th (ppm)	Th/U	Pb (ppm)	com m Pb (%)
T5D21	40	23	b1	12.3	0.4	7.7	2.5	n.s	n.s	0.00191	3.1	0.0076	32.6	0.0515	0.8		X	1721	170	0.10	2.8	2.83
T5D21	3b2b	3	b1	13.3	2.0	13.3	2.0	12.2	102.8	0.00207	14.9	0.0132	15.5	0.0468	1.8	X	X	5622	308	0.05	10.0	0.07
T5D21	2	3	b2	13.7	0.3	8.1	1.1	n.s	n.s	0.00212	2.4	0.0080	13.5	0.0501	0.6		X	5213	272	0.05	9.5	2.84
T5D21	23b2b3	23	b2	13.9	2.1	14.4	2.4	111.9	154.0	0.00215	15.0	0.0143	16.5	0.0483	1.9	X	X	1097	103	0.09	2.0	0.01
T5D21	39	23	c	14.8	0.4	14.8	2.2	n.s	n.s	0.00229	2.7	0.0147	15.2	0.0509	0.7	X	X	1625	175	0.11	3.2	0.57
T5D21	33b1b1	33	b	19.8	2.9	22.0	3.2	266.4	43.4	0.00308	14.8	0.0219	14.9	0.0556	1.0	X		10653	118	0.01	28.2	0.50
T5D21	13	10	c	23.7	0.9	30.3	4.3	n.s	n.s	0.00368	3.6	0.0303	14.4	0.0588	3.6	X		429	2	0.00	1.4	0.00
T5D21	8	6	b	50.7	3.2	18.1	4.7	n.s	n.s	0.00789	6.3	0.0180	26.0	0.0572	1.1			649	12	0.02	4.4	4.97
T5D21	16	12	b	157.4	3.8	166.8	4.8	n.s	n.s	0.02472	2.4	0.1785	3.1	0.0564	0.6			1190	1600	1.34	25.3	0.51
T5D21	34	19	b	264.3	6.2	282.5	6.7	n.s	n.s	0.04185	2.4	0.3208	2.7	0.0567	1.2			3355	85	0.03	120.7	0.14
T5D21	4	5	b	322.1	7.4	326.6	7.4	n.s	n.s	0.05123	2.4	0.3794	2.7	0.0567	0.9			599	18	0.03	26.4	0.38
T5D21	3	5	c	345.3	9.1	358.2	8.7	n.s	n.s	0.05503	2.7	0.4230	2.9	0.0568	0.6			470	76	0.16	22.2	0.13
T5D21	26	15	b	375.7	7.8	405.0	8.0	n.s	n.s	0.06002	2.1	0.4902	2.4	0.0581	0.9			497	53	0.11	25.6	0.00
T5D21	15	12	c	382.0	8.4	399.7	8.3	n.s	n.s	0.06105	2.3	0.4824	2.5	0.0572	0.6			483	407	0.84	25.3	0.00
T5D21	37	20	c	391.0	27.4	461.4	34.4	n.s	n.s	0.06252	7.2	0.5753	9.4	0.0646	6.0			194	54	0.28	10.4	0.00
T5D21	38	20	b	407.4	8.6	425.7	10.1	n.s	n.s	0.06524	2.2	0.5208	2.9	0.0586	1.0			393	111	0.28	22.0	0.09
T5D21	20	13	b	444.5	8.8	460.4	8.4	n.s	n.s	0.07139	2.0	0.5736	2.3	0.0582	0.8			782	73	0.09	48.0	0.00
T5D21	27	16	c	474.5	9.8	491.0	9.5	n.s	n.s	0.07638	2.1	0.6218	2.4	0.0589	0.7			551	93	0.17	36.1	0.00
T5D21	21	14	c	475.1	9.0	503.9	8.0	n.s	n.s	0.07648	2.0	0.6426	2.0	0.0609	0.5			3212	110	0.03	211.1	0.00
T5D21	19	13	c	486.0	10.1	495.5	8.8	n.s	n.s	0.07830	2.2	0.6291	2.3	0.0576	0.5			719	147	0.20	48.4	0.00
T5D21	32	18	b	509.7	9.8	512.3	8.4	n.s	n.s	0.08227	2.0	0.6561	2.1	0.0578	0.5			1461	846	0.58	103.3	0.01
T5D21	10	8	b	545.7	11.8	567.5	10.4	n.s	n.s	0.08834	2.3	0.7487	2.4	0.0625	0.6			654	74	0.11	49.7	0.13
T5D21	1	3	c	587.1	16.5	746.4	15.7	1259.2	12.0	0.09535	2.9	1.0856	3.0	0.0825	0.6			511	56	0.11	41.8	0.00
T5D21	9	8	c	869.5	17.0	887.2	12.5	n.s	n.s	0.14441	2.1	1.3958	2.1	0.0704	0.3			1158	39	0.03	143.6	0.04
T5D21	33	19	c	1003.1	24.6	1479.7	21.3	n.s	n.s	0.16836	2.7	3.2942	2.8	0.1420	0.7			385	263	0.68	55.7	0.03

Table DR4-1

Sample name	spot name	crystal	spot location b: border c: core	Age (Ma) 206/238	± (1σ)	Age (Ma) 207/235	± (1σ)	Age (Ma) 207/206	± (1σ)	206/238	± (%)	207/235	± (%)	207/206	± (%)	Used in concordia	Used in TW	U (ppm)	Th (ppm)	Th/U	Pb (ppm)	comm Pb (%)
T5D20	15	28	b	14,2	0,4	15,8	0,6	n.s	n.s	0,00221	2,6	0,0157	3,6	0,0488	1,3	X	X	5021	64	0,01	9,5	0,00
T5D20	5	42	b2	41,0	0,5	51,4	1,0	n.s	n.s	0,00638	1,2	0,0519	2,0	0,0583	0,7	X	X	1709	88	0,05	9,4	0,00
T5D20	17b2	17	b	43,3	1,7	68,8	6,1	1084,0	158,5	0,00673	3,9	0,0702	9,2	0,0657	2,7	X	X	433	9	0,02	2,5	0,00
T5D20	t5d20ter27	15	b	322,0	6,9	318,4	15,5	291,5	116,6	0,05123	2,2	0,3683	5,7	0,0579	0,9			2732	59	0,02	120,2	0,71
T5D20	4	42	b1	343,7	5,0	301,7	17,9	n.s	n.s	0,05476	1,5	0,3460	6,9	0,0616	0,9			580	35	0,06	27,3	1,91
T5D20	27	7	c	397,7	6,6	427,2	6,8	n.s	n.s	0,06364	1,7	0,5231	1,9	0,0575	0,8			504	91	0,18	27,5	0,00
T5D20	2	43	c	398,6	19,5	433,0	18,8	n.s	n.s	0,06379	5,0	0,5317	5,4	0,0570	1,6			230	169	0,73	12,6	0,00
T5D20	14	28	c2	399,3	5,6	432,3	7,5	n.s	n.s	0,06389	1,4	0,5307	2,1	0,0594	1,1			317	150	0,47	17,4	0,00
T5D20	t5d20ter10	1	b	412,9	17,1	427,8	23,6	509,0	113,1	0,06614	4,3	0,5240	6,8	0,0647	1,9			317	64	0,20	18,0	0,87
T5D20	28b2	28	c1	460,0	18,7	486,9	18,4	615,4	48,6	0,07397	4,2	0,6153	4,8	0,0586	1,3			286	72	0,25	18,1	0,00
T5D20	3	43	b	495,1	7,8	501,2	7,5	n.s	n.s	0,07983	1,6	0,6382	1,9	0,0564	0,9			590	176	0,30	40,5	0,00
T5D20	17c2	17	c	524,0	17,7	594,4	16,0	873,4	14,3	0,08467	3,5	0,7957	3,6	0,0682	0,7			2555	1964	0,77	185,9	0,01
T5D20	8	31	c	594,8	10,0	646,4	9,0	n.s	n.s	0,09666	1,8	0,8901	1,9	0,0665	0,6			754	205	0,27	62,6	0,00
T5D20	26	18	b2	744,3	8,1	792,3	7,0	n.s	n.s	0,12239	1,2	1,1822	1,3	0,0708	0,4			1517	457	0,30	159,5	0,10
T5D20	9	31	b	881,9	10,5	893,4	10,6	n.s	n.s	0,14661	1,3	1,4105	1,8	0,0699	1,2			1124	74	0,07	141,5	0,03
T5D20	t5d20ter15	6	b	1832,3	37,8	2176,7	41,0	2519,3	65,9	0,32874	2,4	7,5314	4,7	0,1910	0,4			1491	177	0,12	421,1	2,68
T5D20	25	18	b1	821,4	6,6	868,7	5,2	991,3	5,1	0,1	0,9	1,35268	0,9	0,0721	0,0			974	276,82	0,3	114	0,00

Table DR4-2

Sample name	crystal	Spot Name	spot location b: border c: core	Age (Ma) 208/232	± (1σ)	208/232	± (%)	238/206	± (%)	207/206	± (%)	Used in TW	U (ppm)	Th (ppm)	206* (ppm)	comm 206 (%)
T5D20	1	1.2	b	15.1	0.4	.00078	2.5	387.10	2	0.051	2	X	26829	54134	59.5	1.4
T5D20	9	9.1	c	15.5	0.4	.00082	5.1	368	4.5	0.0574	2.3	X	31459	68497	29.5	1.5
T5D20	15	15.1	c	15.9	1.0	.00083	5.9	374	2.7	0.0684	2.1	X	7892	87449	18.1	8.0
T5D20	9	9.2	b	16.0	0.8	.00085	8.4	367	7.3	0.05296	1	X	12619	78314	69.7	3.9
T5D20	10	10.1	c	16.0	0.5	.00083	3.0	387	2.6	0.0547	3.2	X	18864	58843	41.9	2.2
T5D20	1	1.1	c	16.0	0.4	.00083	2.4	365.7	2	0.0594	3.1	X	9528	59421	22.4	3.6
T5D20	8	8.2	b	16.1	1.3	.00080	2.7	395	2.6	0.0528	1.3	X	29737	43787	68.4	1.6
T5D20	8	8.1	c b	16.2	0.5	.00084	2.9	379	2.8	0.0687	2.6	X	5418	54716	12.3	7.2
T5D20	4	4.1	c	16.4	0.4	.00083	2.2	357.3	1.9	0.0567	2.7		9568	56866	23.0	2.1
T5D20	14	14.1	c	16.4	0.5	.00087	3.0	343.6	2.8	0.0837	2.8		3363	51064	8.4	14.3
T5D20	13	13.1	c	16.6	0.5	.00087	3.1	366	2.8	0.0651	3.3	X	5423	27168	12.7	4.4
T5D20	11	11.2	b	19.2	0.6	.00100	3.0	317.2	2.8	0.066	2.8		4623	41903	12.5	6.8
T5D20	14	14.2	b	19.5	0.6	.00103	3.4	360.3	2.6	0.0627	1.8	X	14609	67987	34.8	5.3

Table DR5-1

Sample name	crystal	Spot Name	spot location b: border c: core	Age (Ma) 208/232	± (1σ)	208/232	± (%)	238/206	± (%)	207/206	± (%)	populati on	Used in TW	U (ppm)	Th (ppm)	206* (ppm)	comm 206 (%)
T5D21	7	7.1	c	14.3	0.4	.00076	2.9	397.04	2.6	.0570	2.6	Pop1	pop1	13513	45312	29.2	3.3
T5D21	6	6.1	b	14.7	0.5	.00079	2.8	390.72	2.6	.0717	3.0	Pop1	pop1	18805	110978	41.3	6.6
T5D21	8	8.1	c	14.9	0.5	.00078	2.9	390.33	2.7	.0746	2.3	Pop1	pop1	5959	61205	13.1	8.9
T5D21	12	12.1	c	15.0	0.4	.00080	2.8	363.30	2.6	.0615	1.7	Pop1	pop2	14828	76166	35.1	5.0
T5D21	9	9.1	c	15.2	0.5	.00079	3.1	360.12	3.0	.0903	2.4	Pop1	pop2	4034	63137	9.6	11.1
T5D21	10	10.1	c	15.3	0.5	.00080	3.1	332.29	2.8	.1386	2.6	Pop1	pop2	2576	61182	6.7	16.5
T5D21	7	7.2	b	15.5	0.5	.00084	3.0	379.34	2.8	.0660	3.2	Pop1	pop2	13276	54463	30.1	5.7
T5D21	4	4.1	c	15.6	0.5	.00081	2.9	386.30	2.7	.0557	1.4	Pop1	pop2	23970	63432	53.3	1.8
T5D21	1	1.1	b	15.6	0.5	.00082	3.3	381.63	3.1	.0584	1.4	Pop1	pop2	19614	59995	44.2	3.1
T5D21	1	1.3	b	16.2	0.5	.00084	2.8	371.96	2.6	.0557	1.8	Pop2	pop2	16065	65768	37.1	2.8
T5D21	11	11.1	c	16.5	0.5	.00087	2.9	380.10	2.6	.0563	2.4	Pop2	pop2	24918	64191	56.3	2.5
T5D21	1	1.2	c	16.7	0.6	.00086	3.8	373.96	2.7	.0576	1.9	Pop2	pop2	14962	48177	34.4	2.2
T5D21	3	3.1	b	17.2	0.5	.00090	3.0	368.68	2.6	.0571	1.7	Pop2	pop2	21099	69255	49.2	3.2
T5D21	5	5.1	b	17.9	0.6	.00093	3.3	376.30	2.6	.0612	3.3	Pop2	pop2	22657	99376	51.7	3.8

Table DR5-2

Temperature °C	$^{40}Ar/^{39}Ar$	$^{38}Ar/^{39}Ar$	$^{37}Ar/^{39}Ar$	$^{36}Ar/^{39}Ar$ (10^{-3})	^{39}Ar (10^{-14}moles)	$F^{39}Ar$ released	$\%^{40}Ar^*$	$^{40}Ar^*/^{39}Ar$	Age Ma	± 1σ Ma
T5D19b		Biotite		J= 0.009075						
700	48,852	0,209	0,138	181,156	0,02	0,42	-9,60	-4,69	0,00	0,00
750	12,419	0,052	0,104	32,833	0,04	1,24	21,77	2,70	43,73	5,24
800	4,867	0,028	0,074	14,627	0,15	4,73	10,87	0,53	8,64	1,62
850	2,940	0,029	0,022	6,289	0,27	11,10	36,15	1,06	17,31	0,84
900	2,348	0,025	0,008	4,786	0,65	26,47	38,94	0,91	14,91	0,36
950	1,494	0,021	0,006	1,527	0,59	40,29	68,47	1,02	16,67	0,35
1000	1,223	0,020	0,002	0,925	1,53	76,41	76,02	0,93	15,16	0,13
1050	1,552	0,022	0,008	2,006	0,45	86,94	60,55	0,94	15,32	0,38
1100	1,637	0,025	0,013	1,809	0,23	92,45	66,17	1,08	17,65	0,46
1200	3,049	0,029	0,031	8,150	0,14	95,70	20,42	0,62	10,17	0,96
1400	21,351	0,025	0,027	64,925	0,18	100,00	10,06	2,15	34,83	1,91

Temperature °C	$^{40}Ar/^{39}Ar$	$^{38}Ar/^{39}Ar$	$^{37}Ar/^{39}Ar$	$^{36}Ar/^{39}Ar$ (10^{-3})	^{39}Ar (10^{-14}moles)	$F^{39}Ar$ released	$\%^{40}Ar^*$	$^{40}Ar^*/^{39}Ar$	Age Ma	± 1σ Ma
T5D20		Biotite		J= 0.009075						
600	115,497	0,267	0,103	418,754	0,02	0,11	-7,15	-8,26	0,00	0,00
700	46,866	0,118	0,087	140,333	0,02	0,23	11,49	5,38	86,05	14,32
750	12,770	0,052	0,051	35,042	0,07	0,64	18,78	2,40	38,84	3,10
800	5,121	0,032	0,027	14,020	0,30	2,28	18,74	0,96	15,64	0,93
850	2,199	0,027	0,011	5,067	1,03	7,97	31,03	0,68	11,14	0,29
900	1,215	0,026	0,003	1,188	4,79	34,47	69,46	0,84	13,76	0,08
950	1,026	0,025	0,003	0,518	3,46	53,62	83,14	0,85	13,91	0,07
1000	1,118	0,023	0,004	0,771	2,18	65,70	77,84	0,87	14,19	0,10
1050	0,989	0,025	0,056	0,272	4,10	88,36	90,18	0,89	14,54	0,06
1100	1,130	0,025	0,004	1,051	1,57	97,05	70,76	0,80	13,04	0,17
1200	2,192	0,026	0,039	4,706	0,41	99,33	35,76	0,78	12,79	0,53
1400	35,766	0,049	0,080	120,749	0,12	100,00	0,19	0,07	1,13	3,25

Table DR6-1

Temperature °C	$^{40}Ar/^{39}Ar$	$^{38}Ar/^{39}Ar$	$^{37}Ar/^{39}Ar$	$^{36}Ar/^{39}Ar$ (10^{-3})	^{39}Ar (10^{-14}moles)	$F^{39}Ar$ released	$\%^{40}Ar^*$	$^{40}Ar^*/^{39}Ar$	Age Ma	± 1σ Ma
T5D20		Muscovite		J= 0.009075						
600	29,627	0,088	0,065	101,275	0,02	0,13	-1,07	-0,32	0,00	0,00
700	121,145	0,000	0,001	0,338	0,00	0,13	99,90	0,00	0,00	0,00
750	15,856	0,001	0,183	83,769	0,02	0,28	-56,17	-8,91	0,00	0,00
800	6,491	0,024	0,094	16,118	0,06	0,79	26,40	1,71	27,84	7,57
850	3,341	0,030	0,026	8,056	0,15	2,08	28,20	0,94	15,36	1,69
900	2,898	0,020	0,024	5,856	0,41	5,66	39,65	1,15	18,72	0,61
950	1,812	0,014	0,009	3,417	1,19	15,91	43,22	0,78	12,78	0,27
1000	1,112	0,013	0,003	0,830	4,87	57,92	76,17	0,85	13,81	0,05
1050	1,153	0,014	0,005	1,056	2,64	80,66	71,24	0,82	13,40	0,09
1100	1,184	0,014	0,006	0,853	1,47	93,36	77,07	0,91	14,88	0,10
1200	1,632	0,014	0,013	2,279	0,66	99,03	57,54	0,94	15,31	0,24
1400	35,675	0,048	0,070	120,722	0,11	100,00	-0,04	-0,01	0,00	0,00

Temperature °C	$^{40}Ar/^{39}Ar$	$^{38}Ar/^{39}Ar$	$^{37}Ar/^{39}Ar$	$^{36}Ar/^{39}Ar$ (10^{-3})	^{39}Ar (10^{-14}moles)	$F^{39}Ar$ released	$\%^{40}Ar^*$	$^{40}Ar^*/^{39}Ar$	Age Ma	± 1σ Ma
T5D21		Muscovite		J= 0.009545						
700	19,253	0,077	0,016	54,016	0,07	0,11	17,00	3,27	55,49	3,54
750	19,248	0,045	0,007	55,995	0,03	0,16	13,93	2,68	45,60	6,66
800	8,868	0,022	0,023	25,651	0,09	0,31	14,32	1,27	21,74	3,05
833	5,454	0,020	0,036	12,840	0,14	0,56	30,11	1,64	28,06	1,47
866	3,422	0,016	0,018	8,014	0,32	1,09	30,25	1,04	17,74	0,74
900	2,488	0,016	0,012	5,238	0,57	2,05	37,02	0,92	15,79	0,46
933	2,211	0,015	0,011	4,523	1,17	4,00	38,67	0,85	14,66	0,22
966	1,760	0,013	0,005	3,052	2,68	8,50	47,65	0,84	14,39	0,11
1000	1,409	0,013	0,002	1,935	6,16	18,82	57,98	0,82	14,01	0,08
1033	1,150	0,013	0,001	1,113	10,98	37,20	69,67	0,80	13,74	0,05
1066	1,076	0,013	0,002	0,875	9,51	53,13	74,12	0,80	13,69	0,05
1100	1,185	0,013	0,003	1,306	6,33	63,74	65,77	0,78	13,37	0,07
1200	1,055	0,013	0,006	0,774	19,60	96,56	76,45	0,81	13,83	0,04
1400	3,179	0,021	0,651	6,681	2,06	100,00	38,51	1,22	20,97	0,15

Table DR6-2

location	abreviation Fig. 1a	Longitude (°.D)	timing of end of motion on the STDS	based on	references
Sakteng	SK	91.7	After 22-17 Ma ago	Crystallization age of ante kinematic leucogranite dyke from the Sakteng Klippe	Grujic et al. (2002)
Ura	U	90.8	after 15.9 Ma ago	Youngest U/Pb age of Zr rim in deformed leucogranite	Kellet et al. (2009)
			between 11 and 8.6 Ma	Cooling history of the Cheka formation (A/Ar and FT ages)	Age data from Kellet et al. (2009)
Gonta La	G	90.4	After 12.5Ma ago	U/Pb crystallization age (Mz) of ante kinematic Khula Kangri granite	Edwards & Harrison (1997)
			between 11 Ma and 8 Ma	Cooling history from Ar/Ar biot and Mu and Ap FT ages	Ages from Maluski et al. (1988) and Kellett et al. (2009)
Wagye La / Masang kang	W	89.8	After 11.9 Ma ago	U/Pb crystallization age (Mz) of ante kinematic Wagye La granite	Wu et al. (1998)
			After ~12 Ma ago	U/Pb age of zr rim in deformed leucogranite	Age data from Kellet et al. (2009)
Lingshi	L	89.7	After ~16.5 Ma ago	Youngest U/Pb age of zr rim in deformed leucogranite	Kellet et al. (2009)
			between 11.5 and 8 Ma ago	Cooling history from Ar/Ar Mu and Ap FT ages	Age data from Kellet et al. (2009)
Saer	S	87.8	After 16 Ma ago	U/Pb crystaliztion age (Mz) of deformed leucogranites	this study
			After 13.6 Ma ago	Footwall Ar/Ar (Biot and Mu) cooling ages	this study
			Before 11 Ma ago	Crystallization age (Mz) of dyke crosscuting ductile deformation associated with N-S normal fault that post date the	Kali et al. In press
Dzakar Chu	D	87.2	before 20 Ma	U/Pb age (Mz) of undeformed granitic dykes ~1km below the STD	Cottle et al. (2007)
			After 20.9Ma and prior to 16.7	Age of deformed and undeformed leucogranites	Cottle et al. (2009)
Chomolangma	C	86.9	After 16 Ma ago	U/Pb age (Mz) of granitic dykes deformed by the Qomolangma detachement (Rongbuk)	Murphy & Harrison (1999)
			After 14.4 Ma	Cooling history (Ar/Ar and FT) of the yellow band formation	Age data from Sakai et al. (2005), Carosi et al. (1998) and Hodges et al., (1998)
			After 15.2Ma and prior to 12.5 Ma	Age of deformed and undeformed leucogranites ~7 km below the STD	Cottle et al. (2009)
Nyalam	N	86	After 16.8 Ma ago	Crystalization age (Mz) of deformed migmatitic granite	Age data from Scharer et al. (1986)
			Between 14 and 9.7 Ma ago	Cooling (Ar/Ar ages and FT) history	Wang et al. (2006)
XixaPangma	X	85.6	After ~17Ma	U/Pb and muscovite Ar/Ar age of a granite deformed by the STDS	Searle et al. (1997)
			after ~13 Ma	Apparent fast exhumation based on Ar and FT apatite of the Shisha Pangma granite	Searle et al. (1997)
Manaslu	M	84.4	After 19.3 Ma	Crystalisation age (Mz) of the Manaslu granite interpreted as affected by top to the north normal deformation	Guillot et al. (1993) and Searle and Godin (2003)
			Between 19.3 and 16 Ma ago	Ar/Ar cooling ages interpreted as linked to buckling of the STDS	Godin et al. (2006)
			After 13.5 Ma	cooling history Ar/Ar ages of the manuslu interpred as due to exhumation below the STD	Copeland et al. (1990) and Guillot et al. (1994)
western Annapurna / Dhaulagiri	A/D	83.7	After 22 Ma	U/Pb crystalization age of weakly deformed leucocratic dyke at the base of the shear zone	Godin et al. (2001)
			After 13.1 Ma	Ar/Ar cooling ages of main deformation	Godin et al., (2001)
			before 14.3 Ma	Ar/Ar age of hydrothermal muscovites in between the Chame and Phu detachhments atributed to Takhola phase of extension	Coleman and Hodges (1995)
			before 11.8 Ma	Ar/Ar age of hydrothermal muscovites atributed to Takhola grabben	Godin et al. (2001)
Gurla Mandhata	GM	81.3	Before 12 Ma ago	Age of the N-S GM detachment that offset the STDS, based on Th/Pb ages of mz in granites and Ar/Ar cooling ages	Age data from Murphy et al. (2002)
Garhwal (Shivling)	GW	79.0	After 21.9 Ma ago	Mz U-Th/Pb age of the deformed Shivling leucogranite	age data from Harrison et al. (1997) and Searle et al. (1999)
			between 14.2 and 18.9 Ma ago	end of rapid colling from mu K/Ar, Zr FT and ap FT ages	Searle et al. (1999) and Stern et al. (1989)
Garhwal (Gango Tri)	GW	78.9	After 22.4 Ma ago	Mz U-Th/Pb age of the Gangotri leucogranite	Harrison et al. (1997)
			between 2.4 and 18.9 Ma ago	end of rapid colling from Ar/Ar, and Ap FT ages	Sorkabi et al. (1996)
Zanskar (Gulburanjun granite)	Za	77.25	After 19.5 Ma ago	U/Pb age of the anatectic melting in the STDS footwall (Gulburanjun granite)	Dezès et al. (1999) and Walker et al. (1999)
			Between ~19 and ~16 Ma	Decrease of cooling rate from Ar, Rb/sr and FT data	Searle et al. (1999) (rev.); Sorkhabi et al. (1997); and data from Dezès et al. (1999), Walker et al. (1999) and Ferrara et al. (1991)

Table DR7

Data repository bibliography.

Arnaud, N., Tapponnier, P., Roger, F., Brunel, M., Scharer, U., Wen, C., Xu, Z.Q., 2003. Evidence for Mesozoic shear along the western Kunlun and Altyn-Tagh fault, northern Tibet (China). J. Geophys. Res. 108, DOI: 10.1029/2001JB000904

Berger, G.W., York, D., 1981. Geothermometry from Ar-40-Ar-39 Dating Experiments. Geochim. Cosmochim. Acta. 45, 795-811.

Burchfiel, B.C., Zhilang, C., Hodges, K.V., Yuping, L., Royden, L.H., Changrong, D., Jiene, X., 1992. The South Tibetan detachment System, Himalayan Orogen: Extension Contemporaneous with and Parallel to Shortening in a Collisional Mountain Belt., Geological Society of America

Carosi, R., Lombardo, B., Molli, G., Musumeci, G., Pertusati, P.C., 1998. The south Tibetan detachment system in the Rongbuk valley, Everest region. Deformation features and geological implications. J. Asian Earth Sci. 16, 299-311.

Catlos, E.J., Dubey, C.S., Harrison, T.M., Edwards, M.A., 2004. Late Miocene movement within the Himalayan Main Central Thrust shear zone, Sikkim, north-east India. J. Metamorph. Geol. 22, 207-226.

Colchen, M., Le Fort, P., Pêcher, A., 1986. Recherches géologiques dans l'Himalaya du népal. Anapurna, Manaslu, Ganesh, CNRS, Paris.

Coleman, M.E., 1998. U-PB constraints on oligocene-miocene deformation and anatexis within the central Himalaya, Marsyandi valley, Nepal. Am. J. Sci. 298, 553-571.

Coleman, M.E., Hodges, K.V., 1998. Contrasting Oligocene and Miocene thermal histories from the hanging wall and footwall of the South Tibetan detachment in the central Himalaya from Ar-40/Ar-39 thermochronology, Marsyandi Valley, central Nepal. Tectonics. 17, 726-740.

Compston, W., Williams, I.S., Meyer, C.E., 1984. U-Pb geochronology of zircons from lunar breccia 73217 using a sensitive high mass-resolution ion microprobe. J. Geophys. Res. 89, 525-534.

Copeland, P., Harrison, T.M., Lefort, P., 1990. Age and Cooling History of the Manaslu Granite - Implications for Himalayan Tectonics. J. Volcanol. Geotherm. Res. 44, 33-50.

Cottle, J.M., Jessup, M.J., Newell, D.L., Searle, M.P., Law, R.D., Horstwood, M.S.A., 2007. Structural insights into the early stages of exhumation along an orogen-scale detachment: The South Tibetan Detachment system, Dzakaa Chu section, eastern Himalaya. J. Struct. Geol. 29, 1781-1797.

Cottle, J.M., Searle, M.P., Horstwood, M.A.S., Waters, D.J., 2009. Timing of Midcrustal Metamorphism, Melting, and Deformation in the Mount Everest Region of Southern Tibet Revealed by U(-Th)-Pb Geochronology. J. Geol. 117, 643-664.

Dale, J., Holland, T., Powell, R., 2000. Hornblende-garnet-plagioclase thermobarometry: a natural assemblage calibration of the thermodynamics of hornblende. Contrib. Mineral. Petrol. 140, 353-362.

Dalrymple, G., Lanphere, M.A., 1974. Ar-40/Ar-39 Age Spectra of Some Undisturbed Terrestrial Samples. Geochim. Cosmochim. Acta. 38, 715-738.

Daniel, C.G., Hollister, L.S., Parrish, R.R., Grujic, D., 2003. Exhumation of the Main Central Thrust from lower crustal depths, Eastern Bhutan Himalaya. J. Metamorph. Geol. 21, 317-334.

Deloule, E., Chaussidon, M., Glass, B.P., Koeberl, C., 2001. U-Pb isotopic study of relict zircon inclusions recovered from Muong Nong-type tektites. Geochim. Cosmochim. Acta. 65, 1833-1838.

Dezes, P.J., Vannay, J.C., Steck, A., Bussy, F., Cosca, M., 1999. Synorogenic extension: Quantitative constraints on the age and displacement of the Zanskar shear zone (northwest Himalaya). Geol. Soc. Am. Bull. 111, 364-374.

Edwards, M.A., Harrison, T.M., 1997. When did the roof collapse? Late Miocene north-south extension in the high Himalaya revealed by Th-Pb monazite dating of the Khula Kangri granite. Geology. 25, 543-546.

Edwards, M.A., Kidd, W.S.F., Li, J.X., Yu, Y.J., Clark, M., 1996. Multi-stage development of the southern Tibet detachment system near Khula Kangri. New data from Gonto La. Tectonophysics. 260, 1-19.

Ferrara, G., Lombardo, B., Tonarini, S., Turi, B., 1991. Sr, Nd and O isotopic characterization of the Gophu La and Gumburanjun leucogranite (High Himalaya). Schweiz. Mineral. Petrog. Mitt. 71, 31-51.

Godin, L., 2003. Structural evolution of the Tethyan sedimentary sequence in the Annapurna area, central Nepal Himalaya. J. Asian Earth Sci. 22, 307-328.

Godin, L., Brown, R.L., Hanmer, S., 1999. High strain zone in the hanging wall of the Annapuma detachment, central Nepal Himalaya, in: A. Macfarlane, R.B. Sorkhabi, J. Quade, (Eds), Himalaya and Tibet : Mountain Roots to Mountain Tops 328,Special Paper of the Geological Society of America, pp. 199-210.

Godin, L., Gleeson, T.P., Searle, M.P., Ullrich, T.D., Parrish, R.R., 2006. Locking of southward extrusion in favour of rapid crustal-scale buckling of the Greater Himalayan sequence, Nar valley, central Nepal, in: R.D. Law, M.P. Searle, L. Godin, (Eds), Channel Flow, Ductile Extrusion and Exhumation in Continental Collision Zones 268,Geological Society of London Special Publication, London, pp. 269-292.

Godin, L., Parrish, R.R., Brown, R.L., Hodges, K.V., 2001. Crustal thickening leading to exhumation of the Himalayan Metamorphic core of central Nepal: Insight from U-Pb Geochronology and Ar-40/Ar-39 Thermochronology. Tectonics. 20, 729-747.

Grujic, D., Hollister, L.S., Parrish, R.R., 2002. Himalayan metamorphic sequence as an orogenic channel: insight from Bhutan. Earth Planet. Sci. Lett. 198, 177-191.

Guillot, S., Hodges, K., Lefort, P., Pecher, A., 1994. New Constraints on the Age of the Manaslu Leukogranite - Evidence for Episodic Tectonic Denudation in the Central Himalayas. Geology. 22, 559-562.

Guillot, S., Lefort, P., Pecher, A., Barman, M.R., Aprahamian, J., 1995. Contact-Metamorphism and Depth of Emplacement of the Manaslu Granite (Central Nepal) - Implications for Himalayan Orogenesis. Tectonophysics. 241, 99-119.

Guillot, S., Rochette, P., Le Fort, P., Pêcher, A., 1993. The emplacement of the Manaslu granite (Central Nepal): field and magnetic susceptibility constraints, in: P.J. Treloar, M.P. Searle, (Eds), Himalyan Tectonics 74,Geological Society of London Special Publication, London, pp. 413-428.

Harrison, T.M., Grove, M., McKeegan, K.D., Coath, C.D., Lovera, O.M., Le Fort, P., 1999. Origin and episodic emplacement of the Manaslu intrusive complex, central Himalaya. J. Petrol. 40, 3-19.

Harrison, T.M., Lovera, O.M., Grove, M., 1997. New insights into the origin of two contrasting Himalayan granite belts. Geology. 25, 899-902.

Hodges, K., Bowring, S., Davidek, K., Hawkins, D., Krol, M., 1998. Evidence for rapid displacement on Himalayan normal faults and the importance of tectonic denudation in the evolution of mountain ranges. Geology. 26, 483-486.

Hodges, K.V., Parrish, R.R., Housh, T.B., Lux, D.R., Burchfiel, B.C., Royden, L.H., Chen, Z., 1992. Simultaneous Miocene Extension and Shortening in the Himalayan Orogen. Science. 258, 1466-1470.

Hodges, K.V., Parrish, R.R., Searle, M.P., 1996. Tectonic evolution of the central Annapurna Range, Nepalese Himalayas. Tectonics. 15, 1264-1291.

Holland, T., Baker, J., Powell, R., 1998. Mixing properties and activity-composition relationships of chlorites in the system MgO-FeO-Al2O3-SiO2-H2O. Eur. J. Mineral. 10, 395-406.

Holland, T.J.B., Powell, R., 1998. An internally consistent thermodynamic data set for phases of petrological interest. J. Metamorph. Geol. 16, 309-343.

Kellett, D.A., Grujic, D., Erdmann, S., 2009. Miocene structural reorganization of the South Tibetan detachment, eastern Himalaya: Implications for continental collision. Lithosphere. 1, 259-281.

Ludwig, K.R., 2003. Isoplot 3.00 a geochronological toolkit for Microsoft Excel, . Berkley Geoch. Cent. Spec. Pub. 4,

Maluski, H., Matte, P., Brunel, M., Xiao, X.S., 1988. Argon-39-Argon-40 Dating of Metamorphic and Plutonic Events in the North and High Himalaya Belts (Southern Tibet - China). Tectonics. 7, 299-326.

Murphy, M.A., Copeland, P., 2005. Transtensional deformation in the central Himalaya and its role in accommodating growth of the Himalayan orogen. Tectonics. 24, TC4012, doi:4010.1029/2004TC001659.

Murphy, M.A., Harrison, T.M., 1999. Relationship between leucogranites and the Qomolangma detachment in the Rongbuk Valley, south Tibet. Geology. 27, 831-834.

Murphy, M.A., Yin, A., Kapp, P., Harrison, T.M., Manning, C.E., Ryerson, F.J., Ding, L., Guo, J.H., 2002. Structural evolution of the Gurla Mandhata detachment system, southwest Tibet: Implications for the eastward extent of the Karakoram fault system. Geol. Soc. Am. Bull. 114, 428-447.

Newton, R.C., Charlu, T.V., Kleppa, O.J., 1980. Thermochemistry of the High Structural State Plagioclases. Geochim. Cosmochim. Acta. 44, 933-941.

Parrish, R.R., 1990. U-Pb Dating of Monazite and Its Application to Geological Problems. Can. J. Earth Sci. 27, 1431-1450.

Pêcher, A., LeFort, P., 1986. The metamorphism in central Himalaya, its relations with the thrust tectonic. Sciences de la Terre, mémoires (Nancy). 47, 285-309.

Renne, P.R., Swisher, C.C., Deino, A.L., Karner, D.B., Owens, T.L., DePaolo, D.J., 1998. Intercalibration of standards, absolute ages and uncertainties in Ar-40/Ar-39 dating. Chem. Geol. 145, 117-152.

Roddick, J.C., 1978. Application of Isochron Diagrams in Ar-40-Dating Ar-39-Dating - Discussion. Earth Planet. Sci. Lett. 41, 233-244.

Roddick, J.C., Cliff, R.A., Rex, D.C., 1980. The Evolution of Excess Argon in Alpine Biotites - a Ar-40-Ar-39 Analysis. Earth Planet. Sci. Lett. 48, 185-208.

Sakai, H., Sawada, M., Takigami, Y., Orihashi, Y., Danhara, T., Iwano, H., Kuwahara, Y., Dong, Q., Cai, H.W., Li, J.G., 2005. Geology of the summit limestone of Mount Qomolangma (Everest) and cooling history of the Yellow Band under the Qomolangma detachment. Island Arc. 14, 297-310.

Scharer, U., Xu, R.H., Allegre, C.J., 1986. U-(Th)-Pb Systematics and Ages of Himalayan Leucogranites, South Tibet. Earth Planet. Sci. Lett. 77, 35-48.

Searle, M.P., Godin, L., 2003. The South Tibetan Detachment and the Manaslu Leucogranite: A structural reinterpretation and restoration of the Annapurna-Manaslu Himalaya, Nepal. J. Geol. 111, 505-523.

Searle, M.P., Noble, S.R., Hurford, A.J., Rex, D.C., 1999. Age of crustal melting, emplacement and exhumation history of the Shivling leucogranite, Garhwal Himalaya. Geol. Mag. 136, 513-525.

Searle, M.P., Parrish, R.R., Hodges, K.V., Hurford, A., Ayres, M.W., Whitehouse, M.J., 1997. Shisha Pangma leucogranite, south Tibetan Himalaya: Field relations, geochemistry, age, origin, and emplacement. J. Geol. 105, 295-317.
Sorkhabi, R.B., Jain, A.K., Itaya, T., Fukui, S., Lal, N., Kumar, A., 1997. Cooling age record of domal uplift in the core of the Higher Himalayan Crystallines (HHC), southwest Zanskar, India. Proc. Indian Acad. Sci. - Earth Planet. Sci. 106, 169-179.
Sorkhabi, R.B., Stump, E., Foland, K.A., Jain, A.K., 1996. Fission-track and Ar-40/Ar-39 evidence for episodic denudation of the Gangotri granites in the Garhwal Higher Himalaya, India. Tectonophysics. 260, 187-199.
Spear, F.S., 1993. Metamorphic Phase Equilibria and Pressure Temperature Time Paths. 2nd Eds., Mineralogical Society of America, Washington, DC.
Stern, R.A., 1997. The GSC Sensitive High Resolution Ion Microprobe (SHRIMP); analytical techniques of zircon U-Th-Pb age determinations and performance evaluation. . Cur. Res. - Geol. Surv. Can.
Stern, R.A., Amelin, Y., 2003. Assessment of errors in SIMS zircon U-Pb geochronology using a natural zircon standard and NIST SRM 610 glass. Chem. Geol. 197, 111-142.
Tera, F., Wasserburg, G.J., 1972. U-Th-Pb Systematics in 3 Apollo 14 Basalts and Problem of Initial Pb in Lunar Rocks. Earth Planet. Sci. Lett. 14, 281-304.
Vannay, J.C., Hodges, K.V., 1996. Tectonometamorphic evolution of the Himalayan metamorphic core between the Annapurna and Dhaulagiri, central Nepal. J. Metamorph. Geol. 14, 635-656.
Walker, J.D., Martin, M.W., Bowring, S.A., Searle, M.P., Waters, D.J., Hodges, K.V., 1999. Metamorphism, melting, and extension: Age constraints from the High Himalayan Slab of southeast Zanskar and northwest Lahaul. J. Geol. 107, 473-495.
Wang, Y., Li, Q., Qu, G.S., 2006. Ar-40/Ar-39 thermochronological constraints on the cooling and exhumation history of the South Tibetan Detachment System, Nyalam area, southern Tibet, in: R.D. Law, M.P. Searle, L. Godin, (Eds), Channel Flow, Ductile Extrusion and Exhumation in Continental Collision Zones 268,Geological Society of London Special Publication, London, pp. 327-354.
Wang, Y., Wan, J.L., Li, D.M., Li, Q., Qu, G.S., 2001. Thermochronological evidence of tectonic uplift in Nyalam, South Tibetan Detachment System. Bull. Mineral. Petrol. Geochem. 20, 292-294 (in Chinese with english abstract).
White, R.W., Powell, R., Holland, T.J.B., 2007. Progress relating to calculation of partial melting equilibria for metapelites. J. Metamorph. Geol. 25, 511-527.
White, R.W., Powell, R., Holland, T.J.B., Worley, B.A., 2000. The effect of TiO2 and Fe2O3 on metapelitic assemblages at greenschist and amphibolite facies conditions: mineral equilibria calculations in the system K2O-FeO-MgO-Al2O3-SiO2-H2O-TiO2-Fe2O3. J. Metamorph. Geol. 18, 497-511.
Wiedenbeck, M., Alle, P., Corfu, F., Griffin, W.L., Meier, M., Oberli, F., Vonquadt, A., Roddick, J.C., Speigel, W., 1995. 3 Natural Zircon Standards for U-Th-Pb, Lu-Hf, Trace-Element and Ree Analyses. Geostand. Newslett. 19, 1-23.
Williams, C.T., 1996. Analysis of rare earth minerals, in: A.P. Jones, F. Wall, C.T. Williams, (Eds), Rare earth minerals. Chemistry, origin and ore deposits, Mineralogical Society Series 7,Chapman and Hall, London, pp. 327-348.
Wu, C.D., Nelson, K.D., Wortman, G., Samson, S.D., Yue, Y.J., Li, J.X., Kidd, W.S.F., Edwards, M.A., 1998. Yadong cross structure and South Tibetan Detachment in the east central Himalaya (89 degrees-90 degrees E). Tectonics. 17, 28-45.
York, D., 1969. Least Squares Fitting of a Straight Line with Correlated Errors. Earth Planet. Sci. Lett. 5, 320-324.